

**Al<sub>x</sub>Ga<sub>1-x</sub>As/GaAs GRADED INDEX SEPARATE  
CONFINEMENT HETEROSTRUCTURE SINGLE  
QUANTUM WELL LASERS**

**A THESIS**

**SUBMITTED TO THE DEPARTMENT OF PHYSICS  
AND THE INSTITUTE OF ENGINEERING AND SCIENCES  
OF BILKENT UNIVERSITY  
IN PARTIAL FULFILLMENT OF THE REQUIREMENTS  
FOR THE DEGREE OF  
MASTER OF SCIENCE**

**By**

**Mümtaz Korey Bozkurt**

**February 1994**

**TA  
1700  
.B69  
1994**

# Al<sub>x</sub>Ga<sub>1-x</sub>As/GaAs GRADED INDEX SEPARATE CONFINEMENT HETEROSTRUCTURE SINGLE QUANTUM WELL LASERS

**A THESIS**  
**SUBMITTED TO THE DEPARTMENT OF PHYSICS**  
**AND THE INSTITUTE OF ENGINEERING AND SCIENCE**  
**OF BİLKENT UNIVERSITY**  
**IN PARTIAL FULFILLMENT OF THE REQUIREMENTS**  
**FOR THE DEGREE OF**  
**MASTER OF SCIENCE**

Mümtaz Koray BOZKURT

*tarafından bildirilmiştir*

By  
Mümtaz Koray Bozkurt  
February 1994

TA

1700

- B69

1994

B023076

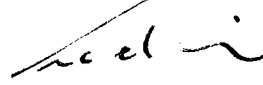
I certify that I have read this thesis and that in my opinion it is fully adequate,  
in scope and in quality, as a thesis for the degree of Master of Science.



---

Prof. Atilla Aydın (Supervisor)

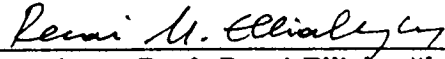
I certify that I have read this thesis and that in my opinion it is fully adequate,  
in scope and in quality, as a thesis for the degree of Master of Science.



---

Prof. Atilla Erelebi

I certify that I have read this thesis and that in my opinion it is fully adequate,  
in scope and in quality, as a thesis for the degree of Master of Science.



---

Assoc.Prof. Recai Ellialtıođlu

Approved for the Institute of Engineering and Science:



---

Prof. Mehmet Baray,  
Director of Institute of Engineering and Science

# Abstract

## $\text{Al}_x\text{Ga}_{1-x}\text{As}/\text{GaAs}$ GRADED INDEX SEPARATE CONFINEMENT HETEROSTRUCTURE SINGLE QUANTUM WELL LASERS

Mümtaz Koray Bozkurt

M. S. in Physics

Supervisor: Prof. Atilla Aydınlı

February 1994

"Stimulated emission of photons could be produced in semiconductors by recombination of carriers injected across a  $p$ - $n$  junction ."

This idea was first suggested by Basov *et al.*<sup>1</sup> in 1961. Soon afterwards diode lasers were first demonstrated at cryogenic temperatures in pulsed operation in 1962 by separate groups in US.<sup>2-5</sup> Until the first use of heterostructures in diode lasers<sup>6-8</sup> in 1969, advances in the diode laser area were not as good as was expected. New era of the diode lasers begin with use of the heterostructures in laser diode technology which allowed them to run at room temperatures in continuous wave operations. Also, introduction of MBE and LPE techniques in crystal growth area supplied the forecoming materials and enabled growing of nanocrystal layers for semiconductor laser diode applications. Reaching to reliable, compact and an efficient components for applications is the major factor which forces the laser diode designs to maturity.

In this work, ridge type Single Quantum Well Graded Index Separately Confined Heterostructure laser diodes which were made by reactive ion etching in  $\text{CCl}_2\text{F}_2$  and lift-off of low temperature PECVD  $\text{SiO}_2$ , is taken from its crystal growth aspects through design and fabrication steps to its characterization.

---

**Keywords :** *Laser diode, single quantum well, graded-index, Gallium Arsenide, plasma enhanced chemical vapor deposition (PECVD).*

# Özet

## $\text{Al}_x\text{Ga}_{1-x}\text{As}/\text{GaAs}$ DEĞİŞKEN KIRILMA İNDİSLİ AYRIK HAPİSLİ HETEROYAPI TEK KUVANTUM KUYULU LAZERLER

Mümtaz Koray Bozkurt  
Fizik Yüksek Lisans  
Tez Yöneticisi: Prof. Atilla Aydınlı  
Şubat 1994

“Yarıiletkenlerde uyarılmış foton yayımı yük taşıyıcılarının  $p$ - $n$  eklemi üzerinden basılması ile elde edilebilir.”

Bu fikir ilk defa Basov ve arkadaşları<sup>1</sup> tarafından 1961 de önerilmiştir. Kısa bir süre sonra düşük sıcaklıklarda darbeli olarak çalışan ilk lazer diyotlar A.B.D. de farklı birkaç grup<sup>2-5</sup> tarafından gerçekleştirilmiştir. Heteroyapıların 1969 da ilk defa lazer diyot yapımında kullanılmasına kadar<sup>6-8</sup> bu alandaki gelişmeler beklendiği ölçüde olmamıştır. Lazer diyot teknolojisinde heteroyapıların kullanımı ile birlikte oda sıcaklığında sürekli çalışabilen lazerlerin elde edilmesi bu teknolojide yeni bir dönem açmıştır. MBE ve LPE tekniklerinin kristal büyütme alanına girmesi, yarıiletken lazer diyot uygulamaları için nanokristal tabakaların büyütülmesine olanak sağlamıştır. Uygulamalar için güvenilir, küçük ve verimli elemanların elde edilmesi lazer diyot tasarım teknolojisini olgunluğa sevk eden faktörlerdir.

Bu çalışmada,  $\text{CCl}_2\text{F}_2$  ile reaktif iyon aşındırma ve alçak sıcaklıklarda plazma ile hızlandırılmış kimyasal fazdan büyütülen  $\text{SiO}_2$  in kaldırılması ile elde edilen sırt şerit tipi tek kuvantum kuyulu değişken kırılma indisli ve ayrik hapisli heteroyapı lazer diyotların, tasarımı, üretimi ve karakterizasyonu aşamaları gerçekleştirilmiştir.

**Anahtar Kelimeler :** *Lazer diyot, tekli kuvantum kuyu, değişken kırılma indisi, Galyum Arsenit, plazma ile hızlandırılmış kimyasal fazdan depolama.*

# Acknowledgement

My sincere thanks are due to my parents for their understanding, moral support, and especially for their patience.

I would like to express my gratitude to my supervisor Prof. Atilla Aydınlı for his constant guidance and encouragement throughout this work. I would like to thank to Assoc. Prof. Recai Ellialtıoğlu for his help. I appreciate the support provided by A.F. Ioffe Physico-Technical Institute and the members of the Optics Laboratory. I wish to express my special thanks to senior research scientist Feodor N. Timofeev.

I would like to thank to my colleague A. Kamuran Türkoğlu for his collaboration. Many thanks to process engineer Murat Güre and to our laboratory technician Güngör Sincer for their help in this work.

This project was performed under the auspices of Ministry of Defense, Undersecretariat for Defense Industries, Grant No: SSM-90-033.50.

.

# Contents

Abstract	i
Özet	ii
Acknowledgement	iii
Contents	iv
List of Figures	vii
<b>1 History and Evolution of Laser Diodes</b>	<b>1</b>
<b>2 Heterojunctions and Quantum Well Lasers</b>	<b>6</b>
2.1 Heterostructures . . . . .	6
2.2 Quantum Well Structures . . . . .	9
2.3 Separate Confinement . . . . .	15
<b>3 Process</b>	<b>17</b>
3.1 Laser Diode Structure . . . . .	17
3.2 Cleaning and Wafer preparation . . . . .	18
3.3 Photolithography . . . . .	20
3.3.1 Photoresists . . . . .	22
3.3.2 Printing . . . . .	22
3.3.3 Experimental . . . . .	23
3.3.4 Process notes . . . . .	27
3.4 Reactive Ion Etching (RIE) . . . . .	28
3.5 Anodic Oxidation . . . . .	36



3.5.1	Process notes . . . . .	37
3.6	PECVD and Lift off of SiO <sub>2</sub> . . . . .	39
3.7	Metalization . . . . .	48
3.7.1	Thinning . . . . .	49
3.7.2	Annealing . . . . .	51
<b>4</b>	<b>Characterization</b>	<b>53</b>
4.1	Laser diode parameters . . . . .	53
4.2	I-V Characterization and Series resistance R <sub>s</sub> . . . . .	54
4.3	Emission spectra of the GRINSCH . . . . .	56
4.3.1	Optical resonant cavity and its modes . . . . .	56
4.3.2	Effect of operating temperature on the emission wavelength	58
4.4	I-P Characterization . . . . .	59
4.4.1	Threshold Current . . . . .	60
4.4.2	Differential quantum efficiency $\eta_D$ . . . . .	65
4.5	Spontaneous Emission and Lasing . . . . .	68
4.6	Far Field Pattern . . . . .	72
4.7	Near Field Pattern . . . . .	75
<b>5</b>	<b>Discussion and Conclusions</b>	<b>78</b>
	<b>Bibliography</b>	<b>81</b>

# List of Figures

1.1	Laser with a Fabry Perot resonator. . . . .	1
1.2	Broad-contact semiconductor laser mounted on heat sink, with lead wire. . . . .	2
2.1	(a) The band diagram of two different disconnected semiconductors 1 and 2, with energies shown relative to the vacuum. The lineup of band structures of lattice-matched semiconductors 1 and 2 forming a heterojunction. It is assumed that materials are undoped and that the effect of charge transfer at the interface is negligibly small. . . . .	7
2.2	Infinitely deep quantum-well energy levels and wave functions. . .	11
2.3	First two bound energy levels and wave functions in a finite quantum well . . . . .	12
2.4	Graphical solution of the energy levels for a finite well Solutions are the intersections of the straight line with slope $k_o^{-1}$ with curves $y = \cos(kL/2)$ (with $\tan(kL/2) > 0$ ; — ; even wavefunctions) or $y = \sin(kL/2)$ (with $\tan(kL/2) < 0$ ; - - - ; odd wavefunctions. . . . .	13
2.5	1-e to 1hh Transition energy vs. Quantum well width . . . . .	14
2.6	1-e to 1lh Transition energy vs. Quantum well width . . . . .	15
2.7	Confined energy levels for a 39 Å thick quantum well. . . . .	16
3.1	Layers and basic energy band diagram of SQW-GRINSCH . . . .	18
3.2	SEM micrograph of SQW-GRINSCH . . . . .	19
3.3	(100) oriented GaAs wafer illustrating cleavage planes and anisotropic as evidenced by a raised mesa and etched slots . . . .	20

3.4	Schematic of refractive optics reduction projection printer. . . . .	21
3.5	Positive and Negative Photoresist behavior after the develop . . .	22
3.6	Mercury lamp output for resist exposure. . . . .	23
3.7	Basic schematic of MJB-3 UV-300 Mask Aligner . . . . .	24
3.8	Basic schematic of RIE . . . . .	28
3.9	Isotropic(left) and anisotropic etching(right) . . . . .	30
3.10	A parallel-plate "Reinberg" style reactor with radial gas flow. . .	31
3.11	Dependence of $U_{ab}$ on RF power (RIE) for $O_2$ and $CCl_2F_2$ ; P=0.8 Pa . . . . .	32
3.12	Profiles of the $5\mu m$ and $12\mu m$ stripes: (a) Before etching (b) After first etching step. . . . .	34
3.13	Etching profiles of the $5\mu m$ and $12\mu m$ stripes after second etching step. . . . .	35
3.14	Anodic oxidation setup. . . . .	37
3.15	Oxide etching characteristic of HCL . . . . .	38
3.16	Parallel plate $\mu p$ -Dp80 plasma reactor in PECVD configuration .	40
3.17	$SiO_x$ Films on Si $p$ -type (100). Data in parenthesis indicate the thickness of the film in Å . . . . .	42
3.18	IR absorption spectra for thermally grown films at 1 atm of dry oxygen at temperatures of 700, 800 and 1000°C. O atom motion for rocking, bending and stretching vibrations are also indicated .	43
3.19	$SiO_x$ -24 absorption spectra . . . . .	44
3.20	RF power (W) vs. Growth Rate (Å/min) . . . . .	47
3.21	Thinning characteristic of GaAs wafers in Ammonia sol.+ $H_2O_2$ (1:10) . . . . .	50
4.1	I-V Characteristic of the GRINSCH Laser Diode . . . . .	55
4.2	Lasing emission spectra of the GRINSCH laser diode . . . . .	57
4.3	Dependence of the band-gap energy of GaAs on temperature. . .	58
4.4	I-P Measurement setup . . . . .	59
4.5	I-P characteristic of GRINSCH . . . . .	60
4.6	$J_{th}$ vs. L (a) For $5\mu m$ stripe width (b) For $12\mu m$ stripe width . .	62

4.7	$I_{th}$ vs. $L$ (a) For $5\mu\text{m}$ stripe width (b) For $12\mu\text{m}$ stripe width . . .	63
4.8	Schematic of the waveguide and reference coordinates. . . . .	64
4.9	$1/\text{Differential Quantum Efficiency } 1/\eta_D$ vs. cavity length $L$ , (a) For $5\mu\text{m}$ stripe width (b) For $12\mu\text{m}$ stripe width. . . . .	66
4.10	Spontaneous emission spectra at different cavity lengths. Peak positions of the spectra are shown by rectangles. . . . .	68
4.11	Spontaneous emission spectra at $804\mu\text{m}$ cavity length is showing two transitions between the edges of the $1e-1lh$ subbands and $1e-1hh$ subbands. . . . .	69
4.12	Lasing emission spectra of GRINSCH at two different current values.	70
4.13	Alignment setup for far field measurement . . . . .	73
4.14	Lateral Far Field patterns for GRINSCH laser diodes. (a) $L=563\mu\text{m}$ $w=5\mu\text{m}$ (b) $L=429\mu\text{m}$ $w=12\mu\text{m}$ . . . . .	74
4.15	Transverse Far Field pattern for $563\mu\text{m}$ long $5\mu\text{m}$ stripe width laser diode. . . . .	75
4.16	Near field measurement setup . . . . .	76
4.17	Near Field pattern of the GRINSCH laser diode, $L=563\mu\text{m}$ $w=5\mu\text{m}$	77

# Chapter 1

## History and Evolution of Laser Diodes

The basic structure of a laser consists of an amplifying medium with inverted population between two mirrors  $M_1$  and  $M_2$  (figure 1.1). The two mirrors constitute a Fabry Perot resonator which confines light at a resonant frequency. Beside Bragg reflectors, diffraction gratings and plane mirrors can also be used internally and externally in such a configuration.

In normal state of the medium there are more electrons in the lower level than in the upper one and stimulated emission and absorption occur simultaneously. If medium is excited by an appropriate method so that upper level contains more

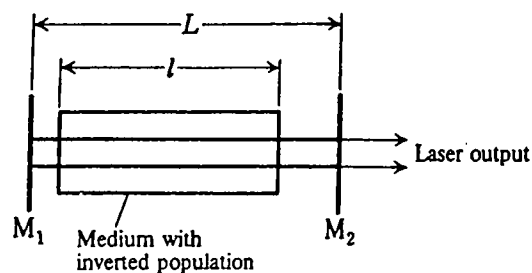
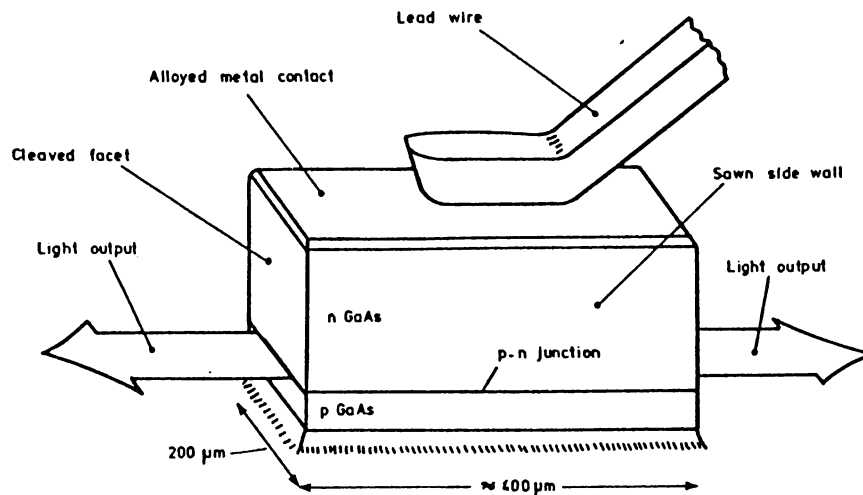


Figure 1.1: Laser with a Fabry Perot resonator.



**Figure 1.2:** Broad-contact semiconductor laser mounted on heat sink, with lead wire.

electrons than the lower one (population inversion) light incident on the medium will be amplified by stimulated emission. Population inversion is obtained in semiconductor injection lasers easily by injecting current through the contacts.

First injection lasers were made from rectangular shaped GaAs  $p$ - $n$  junctions diffused in planar form. Output connections were taken from the top and metal base where the chip was set (figure 1.2). When current is injected into such a structure, like in normal  $p$ - $n$  diode, minority carriers (electrons) come to the junction where thickness is on the order of the diffusion length of the electrons, and they recombine with the majority carriers (holes) and light is emitted. Stimulated emission starts in the junction area when the current density reaches to a sufficient level (threshold level).

Because of the index of refraction difference between the GaAs and air at the cleaved facets (cleaved mirror faces) light is confined inside the medium selecting its Fabry Perot resonance frequency. High rate of stimulated emission in semiconductors allows us to choose the length of Fabry Perot as small as a few hundred microns. Today's semiconductor lasers are based on the same  $p$ - $n$

junction principle and they are represented by the diode symbol.

In such structures threshold current densities lie in the range of 35–100 kA/cm<sup>2</sup>. This high current originates from the high density of states in valence and conduction bands in the bulk material. However light is by no means confined to the area of inversion. Also one can not define an exact region of inversion for the carriers.

Putting additional layers of higher bandgap materials to each side of GaAs *p-n* junction was proposed by Kroemer<sup>9</sup> and Alferov and Kazarinov.<sup>10</sup> Such a design provided the confinement of injected carriers to the active region (*p-n* junction area) and substantially increased the confinement of light to the same region. Injected carriers are kept in the active region by the difference of bandgap energies while inverse relationship between bandgap energy and refractive index gives us the definition of a waveguide for generated light. MBE and LPE crystal growth techniques enabled the growth of higher bandgap ternary elements to be used in laser diodes. Confinement of carriers and the light substantially increased the rate of inversion resulting in a decrease of threshold currents. If higher bandgap material is grown to one side of the active region this design is called single heterostructure, suitable for high power outputs. If the higher bandgap material is grown to either sides of active region it is called double heterostructure, which is suitable for low threshold currents and continuous wave operations.

One of the important things in semiconductor laser diodes is to limit the spread of injected carriers and lasing emission in the plane parallel to the junction. This is achieved by confining the carriers to narrow stripes (from few microns to few tens of microns) aligned along the axis of the laser. To stop carriers outside the stripe areas, different insulating techniques can be used. One such a configuration is called stripe geometry lasers. Dielectric deposition is one of the famous ways to achieve this geometry. In buried type structures proton bombardment can also be used as a process step.

Most of the III-V semiconductors has the inverse relation between refractive index and their bandgaps. Using this fact, contemporary technology offers real confinement of light into active region. By changing the atomic composition of

materials in MBE, energy gaps and refractive indices can be adjusted. If one puts multilayers of such materials step by step to each side of active region, refractive index of the confining layers can be adjusted in the desired shape to form the waveguide. This technique is called index-grading.

With the advent of novel crystal growth techniques such as Molecular Beam Epitaxy (MBE), Metalorganic Chemical Vapor Deposition (MOCVD) and alike, active region thicknesses went down to quantum sizes and new type of semiconductor laser diodes, QW lasers, are fabricated by this means.

These lasers show a number of interesting properties that distinguish them from other types of junction lasers. Their most important characteristics include the following features; low density of the threshold current Tsang<sup>11</sup> 1981, Fujji *et al.*<sup>12</sup> 1984, the small variation of the threshold current with temperature Chin *et al.*<sup>13</sup> 1979, Hess *et al.*<sup>14</sup> 1980, Arakawa and Sakaki<sup>15</sup> 1982, possibility of tuning the emitted wavelength over a wide range, extending up to 100 nm, by varying the driving current, good dynamic characteristics, Arakawa *et al.*<sup>16</sup> 1984, Arakawa and Yariv.<sup>17</sup>

In the initial stage of the QW laser studies Liquid Phase Epitaxy (LPE) was used in layer growths. Good quality single QW lasers were fabricated by Rezek *et al.*<sup>18</sup> by using LPE in 1977. Historically, the first QW lasers of really satisfactory performance have been fabricated by the MOCVD technique by Dupuis and Dapkus<sup>19</sup> and Dupuis *et al.*<sup>20</sup> Kazarinov and Tsarenkov<sup>21</sup> (1976) show theoretically that using index grading technique in the confining layers lowers the threshold currents of the conventional separate confinement structures.

In 1981 Tsang<sup>11</sup> used MBE growth technique in fabrication of multilayer GaAs/Al<sub>x</sub>Ga<sub>1-x</sub>As lasers with threshold current densities of the order of 800 A/cm<sup>2</sup>, which are comparable with the values obtained in the conventional Double Heterostructure Lasers containing Al<sub>x</sub>Ga<sub>1-x</sub>As confining layers with a similar Al content. Gain guided stripe-geometry quantum well lasers operating in continuous wave mode at room temperature with 30 mA threshold current were demonstrated by Tsang.<sup>11</sup>

Hersee *et al.*<sup>22</sup>(1980) used MOCVD technique in fabricating QW lasers of



special design, in which the confining layers of varying composition enhance the efficiency of the carrier capture by the active region. In this study threshold current densities below 300 A/cm<sup>2</sup> was achieved.

In parallel with these studies a model on threshold current in QW lasers was proposed by Dutta<sup>23</sup> (1982) and an accurate model for the gain in QW structure was shown by Asada *et al.*<sup>24</sup> (1985). The effect of gain saturation at high injection currents by Arakawa and Yariv<sup>25</sup> (1986) and the relation between the threshold current and width of the active region layer by Hersee *et al.*<sup>26</sup> (1984) have been confirmed. Single quantum well broad contact GRINSCH lasers with 380-1125  $\mu\text{m}$  cavity length, made by MBE have been reported by Tsang<sup>27</sup> to show threshold current densities ranging from 250 A/cm<sup>2</sup> to 160 A/cm<sup>2</sup> with external incremental quantum efficiencies from 32 to 40 % (one mirror efficiency). Stripe contact GRINSCH lasers of 5  $\mu\text{m}$  stripe width and 380  $\mu\text{m}$  cavity length giving 10 mW per mirror in cw operation have also been demonstrated by Tsang and Hartman<sup>32</sup> (1983). In buried type GRINSCH lasers 2.5 mA threshold current has been reported by Tsang,<sup>27</sup> and Derry *et al.*<sup>30</sup>(1987) have been fabricated lasers with submilliampere threshold currents. Sheally<sup>29</sup> demonstrated superlattice GRINSCH lasers operating in the range of 700 to 845 nm with high efficiency 40 % (one mirror)(1988). Al<sub>x</sub>Ga<sub>1-x</sub>As/GaAs single QW ridge type GRINSCH lasers with power outputs of 425 mW (one mirror) at 856 nm were fabricated, and 428 nm frequency-doubled output of 41 mW was demonstrated by Jaeckel *et al.*<sup>28</sup>

## Chapter 2

# Heterojunctions and Quantum Well Lasers

### 2.1 Heterostructures

In semiconductor literature, when two different semi-infinite semiconductor crystals are joined together, the interface is called heterojunction and the resultant structure is the heterostructure. Crystal structure and the crystal potential doesn't change in bulk areas and abrupt change is seen only at the heterojunction. This is an assumption for the cases in which lattice constants of the materials differ very little for similar materials. By this assumption lattice constant can be taken as a parameter for semiconductors forming heterostructures. Fortunately most of the important semiconductors have zinc-blende and diamond symmetry and are therefore quite compatible provided the lattice constants are similar.

Relative positions of constituent band structures of the heterojunction system provides the band offsets (potential step at the interface figure 2.1). Since mean electron charge density must be the same for both sides of the interface, Fermi energy which depends on it lies in the middle of the gap. Small differences in electron density due to different lattice constants are removed by charge transfer across the interface.

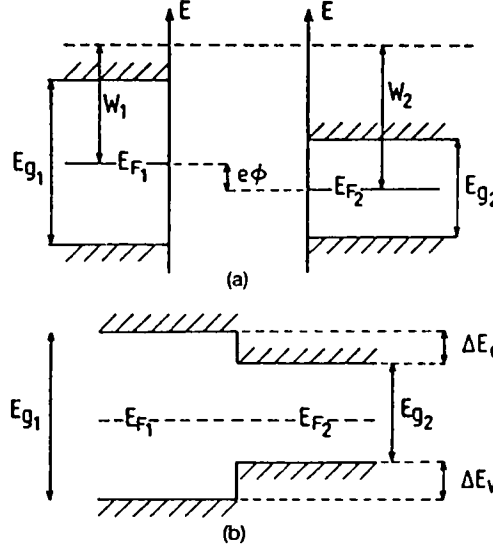


**Figure 2.1:** (a) The band diagram of two different disconnected semiconductors 1 and 2, with energies shown relative to the vacuum. The line-up of band structures of lattice-matched semiconductors 1 and 2 forming a heterojunction. It is assumed that materials are undoped and that the effect of charge transfer at the interface is negligibly small.

To get valence band-offset  $\Delta E_v$ ,

$$\Delta E_v = (E_{g1} - E_{g2})/2$$

If we attempt to use this model and above expression directly for conduction band-offset it fails since conduction band has several minima and in some cases indirect gaps being smaller than direct ones. Once we obtain the valence band offset  $\Delta E_v$  conduction band offset  $\Delta E_c$  is,

$$\Delta E_c = |E_{g1} - E_{g2}| - |\Delta E_v|$$

$E_{g1}$  and  $E_{g2}$  are now the experimental values of the fundamental gaps of the two bulk constituents. If both constituents are direct gap materials, above expression is enough to find  $\Delta E_c$ , subtraction of the energies of the conduction minima that are alike. In our consideration electron passes at the interface from  $\Gamma$  to  $\Gamma$  or X to X valleys even though in some cases X lies below  $\Gamma$ .

For electrons  $\Gamma$  to X valley transfer cannot be used at the interface since abrupt change of electron momentum must take place.<sup>33</sup> Probability of a  $\Gamma$  electron approaching the interface and seeing the X valley is very small. In this way, electron interaction at the interface can be modeled as a reflection from a step-like barrier. By using empirical bulk material energy gap values and lattice constants,<sup>34</sup> band offsets for any pair of heterostructures which have small lattice mismatches can be found. Some of the experimental constants for GaAs and  $\text{Al}_x\text{Ga}_{1-x}\text{As}$  are given in the table below.

	GaAs	$\text{Al}_x\text{Ga}_{1-x}\text{As}$
Lattice constant $a(\text{\AA})$	5.6533	$5.6533 + 0.0078x$
Bandgap Energy $E_g$ (eV) $\Gamma$ valley minima	1.424	$1.424 + 1.247x$ from $x=0$ to $x=0.45$ $1.900 + 0.125x + 0.143x^2$ from $x=1$ to $x=0.45$
Static dielectric constant $\epsilon_s$	13.18	$13.18 - 3.12x$
High Frequency dielectric constant	10.89	$10.89 - 2.73x$
LO phonon energy (meV)	36.25	$36.25 - 6.55x + 1.79x^2$ GaAs type $44.63 + 8.78x - 3.32x^2$ AlAs type
Atomic Structure(Zinc Blende)	Binary	Ternary

## 2.2 Quantum Well Structures

As we mentioned in evolution of the laser diodes, if we grow a very thin layer of material A (such as GaAs) between two thick higher bandgap material B (such as  $\text{Al}_x\text{Ga}_{1-x}\text{As}$ ) these three layers form a double heterostructure. In such a structure higher bandgap materials must be thicker than the penetration length of the confined wave function in the active region. Active region GaAs layer acts as a quantum well if its thickness is in the limits of seeing the quantum size effect.<sup>36,37</sup> This effect can be seen in GaAs active layer if one of its dimensions can be set much smaller than the others ( $L_x \ll L_y, L_z$ ) while comparable with the electron's de Broglie wavelength  $\lambda_b$ . In case QW width is not comparable with de Broglie wavelength  $\lambda_b$ , electrons experience scatterings before the barriers and they can lose their phases and no quantization is seen.

The de Broglie wavelength is given by  $\lambda_b = \hbar/p$  and is estimated to be of the order of 100 Å. For the band offset  $\Delta E_c = 0.1$  eV and effective mass  $m^*$  of 0.1  $m_o$  (where  $m_o$  is the rest mass of the electron) mean free path  $L_z$  of an electron is given by  $L_z = \langle v \rangle / \tau$  where  $\tau$  is the average time between two successive collisions, on the order of  $10^{-13}$  sec.

Average velocity  $\langle v \rangle$  is given by;

$$\langle v \rangle = \sqrt{\frac{2E}{m^*}}$$

for  $\langle v \rangle \sim 5 \times 10^7$  cm/s  $L_z$  is calculated as 500 Å and the de Broglie wavelength for this case;

$$\lambda_b = \frac{2\pi}{k} = 2\pi \sqrt{\frac{\hbar^2}{2Em^*}} = 2\pi a_o \sqrt{\frac{R_y m_o}{Em^*}}$$

where  $a_o = 0.53$  Å,  $R_y = 13.6$  eV yields  $\lambda_b \cong 100$  Å.

From the above calculation mean free path of 500 Å shows an approximate limit between bulk and quantum well behaviors for seeing the quantization. Electron motions perpendicular to the heterojunction are quantized in the x-direction. Motion in other directions can be thought of as two dimensional

electron gas. Energy levels in conduction band can be calculated quite easily in the approximation of envelope wave function, using Kane model.<sup>38,39</sup> It is the same assumption that we used in describing the heterojunctions band offsets. Interface potential is localized in geometrical junction and does not mix the band-edge wave functions but only shifts them. By this assumption electron wave function takes the approximate form of,

$$\Psi = \sum_{A,B} e^{i\vec{k}_\perp \cdot \vec{r}} u_{c\vec{k}}^{A,B}(\vec{r}) \chi_n(z)$$

where  $z$  is the growth direction,  $\vec{k}_\perp$  is the transverse electron wave vector,  $u_{c\vec{k}}(\vec{r})$  is the Bloch wave function in the  $A$  or  $B$  material and  $\chi_n(z)$  is the envelope wave function. They form a Schrödinger-like equation.

$$\left( -\frac{\hbar^2}{2m^*(z)} \frac{\partial^2}{\partial z^2} + V_c(z) \right) \chi_n(z) = \varepsilon_n \chi_n(z)$$

where  $m^*(z)$  is the electron effective mass of the  $A$  or  $B$  material.  $V_c(z)$  is the energy level of the bottom of the conduction bands.  $\varepsilon_n$  is the confinement energy of the carriers. The continuity conditions at the interfaces are that  $\chi_n(z)$  and  $[1/m^*(z)][\partial\chi_n(z)/\partial z]$  should be continuous. In infinitely deep well approximation, solution to Schrödinger-like equation is simple. The wave function must be zero at the interfaces  $A$ - $B$  and is seen only in the material  $B$ . Which is the same as particle in a box problem for one dimension. Wavefunctions are given by sine functions (figure 2.2),  $\sim \sin(n\pi z/L)$ ,  $n$  being an odd or even integer. Corresponding confinement energy levels  $\varepsilon_n$  is simply  $n^2(\pi^2\hbar^2/2m^*L^2)$ .

In real world it is obvious that our quantum-well will not be an infinite one instead a finite. With these boundary conditions the Schrödinger-like equation, can be exactly solved to yield the wave functions and energies. The problem has an inversion symmetry around the center of the well now taken as the center of coordinates (figure 2.3).

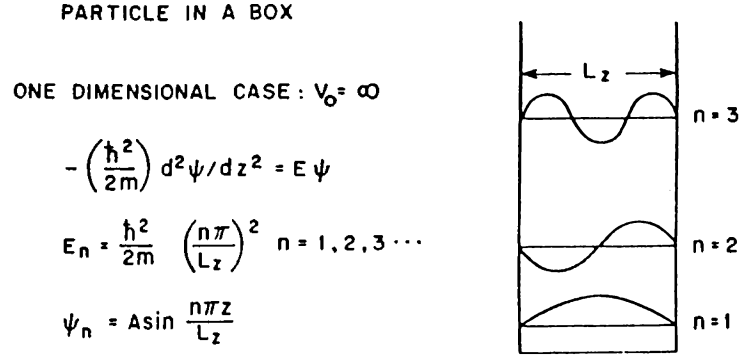


**Figure 2.2:** Infinitely deep quantum-well energy levels and wave functions.

Wave functions can be even or odd. Even functions can be written as,

$$\begin{aligned} \chi_n(z) &= A \cos(kz) & \text{for } |z| < L/2 \\ &= B \exp[-\kappa(z - L/2)] & \text{for } z > L/2 \\ &= B \exp[+\kappa(z + L/2)] & \text{for } z < -L/2 \end{aligned}$$

or the odd functions as,

$$\begin{aligned} \chi_n(z) &= A \sin(kz) & \text{for } |z| < L/2 \\ &= B \exp[-\kappa(z - L/2)] & \text{for } z < L/2 \\ &= B \exp[+\kappa(z + L/2)] & \text{for } z < -L/2 \end{aligned}$$

where

$$\epsilon = \frac{\hbar^2 k^2}{2m_A^*} - V_0 \quad \epsilon = -\frac{\hbar^2 \kappa^2}{2m_B^*} \quad -V_0 < \epsilon < 0$$

For the solution of even function, the continuity conditions at  $z = \pm L/2$  yield,

$$A \cos(kL/2) = B \quad (k/m_A^*) \sin(kL/2) = \kappa B/m_B^*$$

Therefore we get two transcendental equations:

$$(k/m_A^*) \tan(kL/2) = \kappa/m_B^*$$

and for odd solution similarly,

$$(k/m_A^*) \cot(kL/2) = -\kappa/m_B^*$$

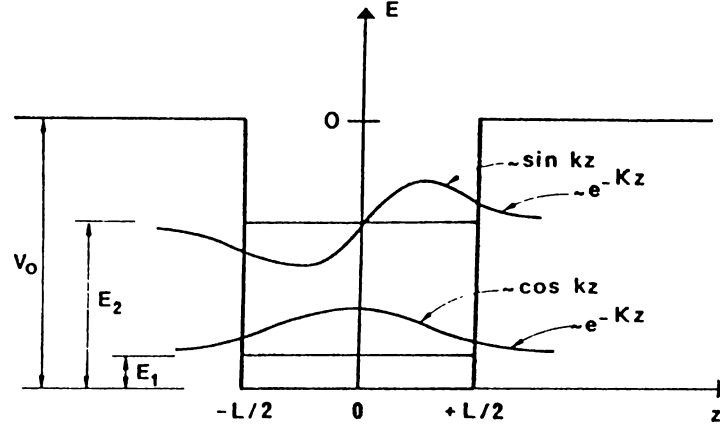


**Figure 2.3:** First two bound energy levels and wave functions in a finite quantum well

These transcendental equations can be solved numerically or graphically. Simple graphical solution can be given if  $m_A^* \approx m_B^*$ . For this condition above equations take the following form.

$$\cos(kL/2) = k/k_o \quad \text{for} \quad \tan(kL/2) > 0$$

$$\sin(kL/2) = k/k_o \quad \text{for} \quad \tan(kL/2) < 0$$

where

$$k_o = \sqrt{2m^*V_o/\hbar^2}$$

Graphical solutions are given in figure 2.4. These solutions yield the following results: number of confined levels in a finite well will be limited and there will always be a one bound state whatever the QW width or attractive potential. Number of confined levels increases as QW depth (band off-set at the heterojunction) or QW width (active layer thickness) is increased. Wave functions are not defined only in the QW, they are continuous at the heterojunction interface and showing decaying exponential characteristics in the confining layers. These exponential tails of the wave-functions are the result of electrons tunneling to the confining layers. That's why instead of wave function itself, its derivative is used for continuity conditions.



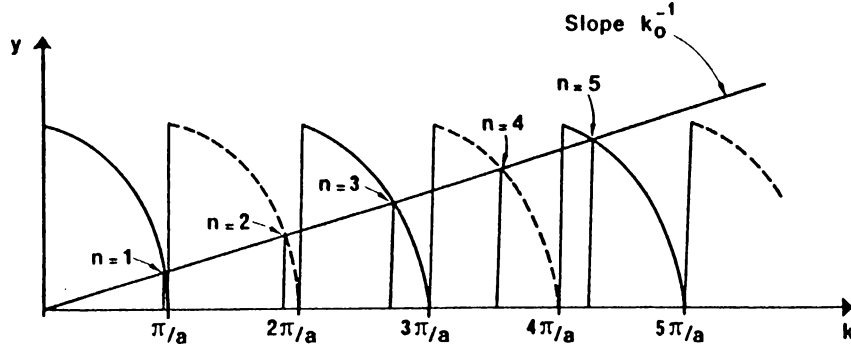


**Figure 2.4:** Graphical solution of the energy levels for a finite well. Solutions are the intersections of the straight line with slope  $k_0^{-1}$  with curves  $y = \cos(kL/2)$  (with  $\tan(kL/2) > 0$  ; — ; even wavefunctions) or  $y = \sin(kL/2)$  (with  $\tan(kL/2) < 0$  ; - - - ; odd wavefunctions).

In figure 2.5 and figure 2.6 solutions for confined energy levels are drawn with respect to the quantum well width in conduction and valence bands. Sixty percent of the energy-gap difference between  $\text{Al}_{0.3}\text{Ga}_{0.7}\text{As}$  and GaAs is taken for the conduction band off-set, while forty percent of it, is used for the valence band off-set.<sup>40</sup> Experimental energy gaps at  $T=300$  K are used and no dopings are considered for GaAs and  $\text{Al}_{0.3}\text{Ga}_{0.7}\text{As}$  layers. In conduction band calculations of the confined electron levels, effective mass of electron, in valence band calculations effective mass of heavy and light holes in the  $\Gamma$  valley of GaAs are used.

From the calculations we can say that for heavy holes there will be no  $2hh$  confined energy level below qw width of  $d=20$  Å and there will be no  $2lh$  state below the QW width of  $d=53$  Å.  $2e$  state does not exist below 50 Å QW width. These calculations show that active layer thickness must be optimized since for low threshold currents number of the energy levels must not be high implying thin active regions whereas for good carrier confinement this thickness must be larger than the average diffusion length of carriers.

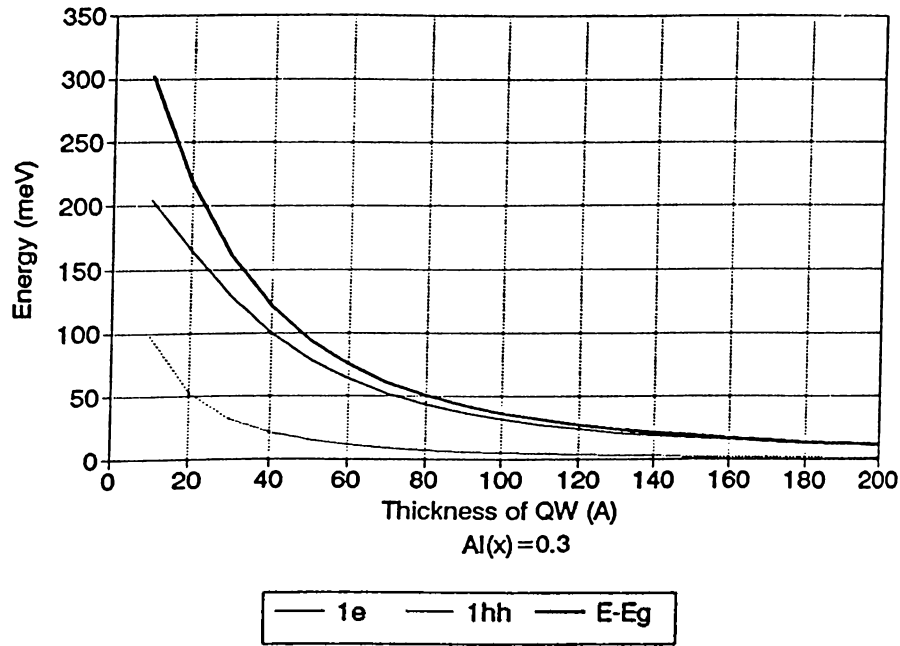


Figure 2.5: 1-e to 1hh Transition energy vs. Quantum well width

Calculated confined energy levels and allowed optical transitions for our GRINSCH SQW of well thickness 39 Å are shown in figure 2.7. In this calculation quantum well and the confinement layers were taken as undoped, assumption of infinitely long confinement layers were used. Band offsets were taken as 60 % conduction and 40 % valence band.

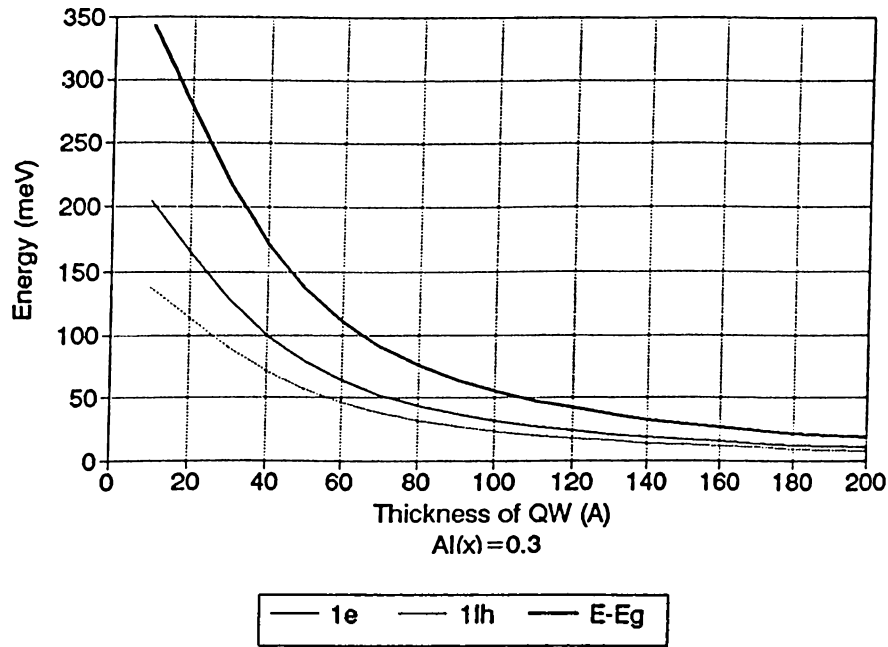


Figure 2.6: 1-e to 1lh Transition energy vs. Quantum well width

## 2.3 Separate Confinement

Normally charge carriers (electrons for conduction, holes for valence bands) are easily confined to the region of quantum well. Only some of them that have finite tunneling probability can penetrate into outer regions. Even though the carriers are confined in this thin layer, generated light can not be confined in this region. As an example, for light generated at  $0.8\mu\text{m}$ , wavelength of the light in the medium can roughly be estimated by dividing it into intrinsic GaAs index of refraction resulting  $0.23\mu\text{m}$ . Thickness of QW is much smaller than this value. Because of this reason enough thick confining layers with lower index of refraction are put to each side of the active region. In this way confinement is achieved electrically and optically in different areas.

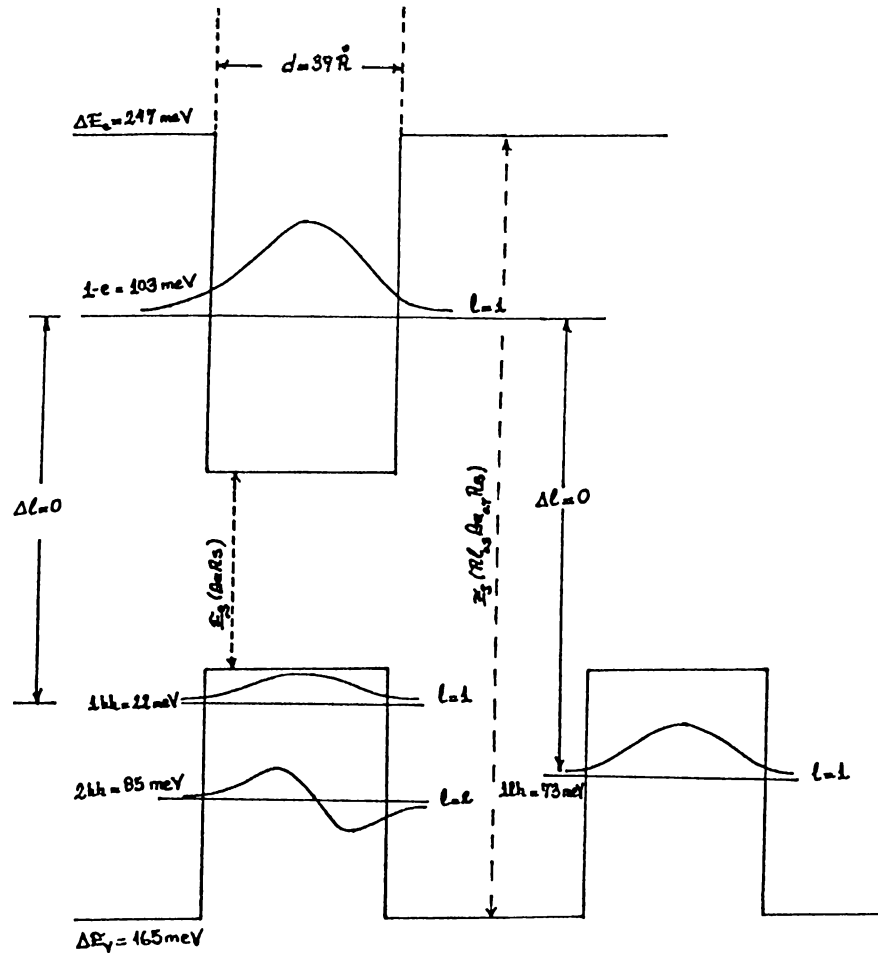


Figure 2.7: Confined energy levels for a 39 Å thick quantum well.

# Chapter 3

## Process

### 3.1 Laser Diode Structure

Laser diodes were fabricated from an MBE grown graded index separate confinement heterostructure. This structure consists of the following layers (figure 3.1). First, over GaAs (001) substrate a  $0.5\mu\text{m}$  thick  $n$ -type GaAs buffer layer has been grown. Normally these kind of layers are grown to increase surface quality and to obtain defect free surfaces for further growths. Most of the dislocations and cracks that can penetrate into the structure are stopped in this region. Following this buffer layer a  $1\mu\text{m}$  thick  $n$ -type  $\text{Al}_x\text{Ga}_{1-x}\text{As}$  intermediate layer has been grown.  $1.5\mu\text{m}$  thick  $n$ -type  $\text{Al}_x\text{Ga}_{1-x}\text{As}$  layer with  $x=0.6$  has been grown as a first confining layer. On two sides of the intrinsic active GaAs region of thickness  $39\text{ \AA}$ ,  $0.2\mu\text{m}$  thick graded index  $\text{Al}_x\text{Ga}_{1-x}\text{As}$  regions with  $x$  changing from 0.6 to 0.3 have been grown. This graded index layer acts in beam shaping of the generated light.  $p$ -type  $1.1\mu\text{m}$  thick  $\text{Al}_x\text{Ga}_{1-x}\text{As}$  layer with  $x=0.6$  has been grown as the second confining layer. To obtain good results in ohmic contact, final  $0.1\mu\text{m}$  thick  $p$ -type degenerately doped GaAs has been grown as a contact layer. Thickness control of the samples were done by a JEOL-JSM 6400 scanning electron microscope. SEM micrograph for GRINSCH is given in figure 3.2.

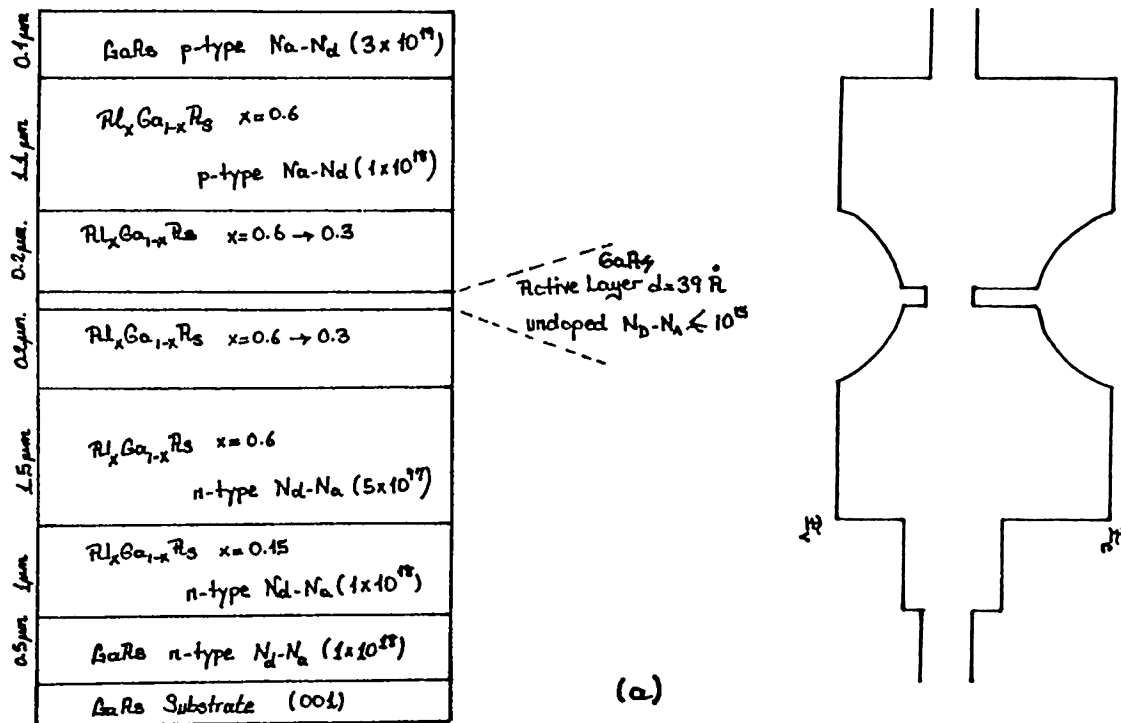


**Figure 3.1: Layers and basic energy band diagram of SQW-GRINSCH**

### 3.2 Cleaning and Wafer preparation

Under clean-room conditions environmental effects on the wafer cleanliness is maximized and well controlled. By using continuous laminar air flows and high efficiency particle attenuation filtering, particles which may cause device failure problems are eliminated from the clean room areas.

In Advanced Research Laboratories (Bilkent) lasers are fabricated under class-100 enviromental conditions. Throughout the fabrication steps and wafer handling all of the samples are kept at 21°C, 24 Pa pressure and 45% relative humidity. All the lithography steps are carried out under yellow safe light.

There are many ways of cleaning and individually they aim at different types of residuals. Generally one can divide the cleaning into two general parts as mechanical cleaning and chemical cleaning. In our process we used both ways in subsequent applications. First, samples are cut into 2 cm by 2 cm square shape

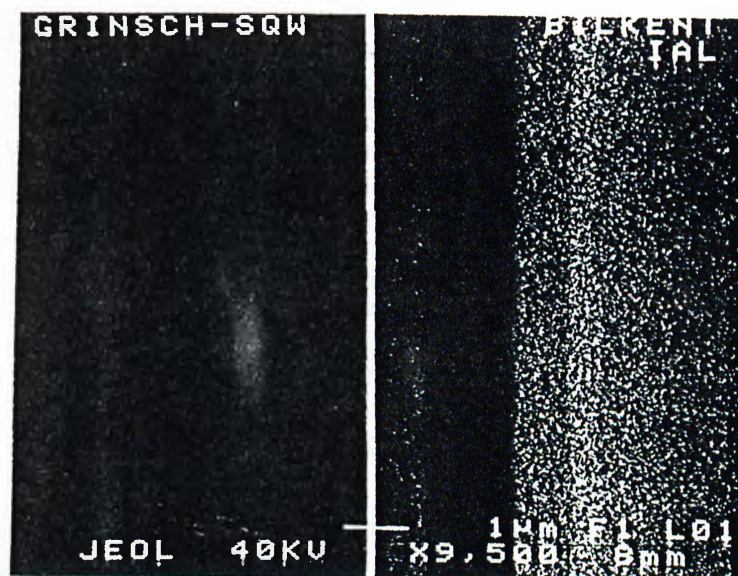
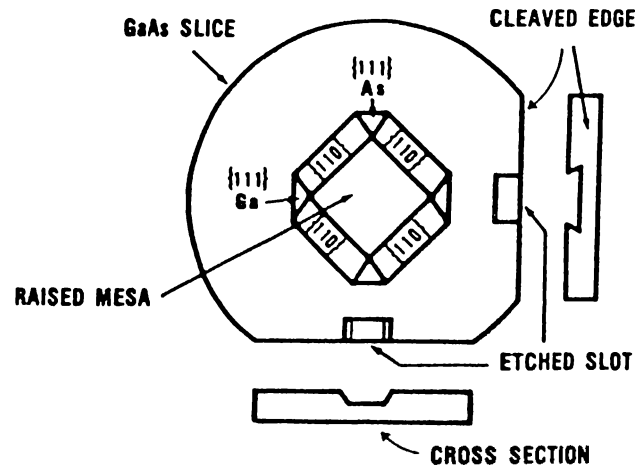


Figure 3.2: SEM micrograph of SQW-GRINSCH

after orientation of their major axis  $\langle 100 \rangle$ . This way is chosen since some of the samples were processed by chemical wet etching, (orientation is important since different crystal directions of GaAs give different chemical etching profiles<sup>41</sup> figure 3.3); while others were processed by dry reactive ion etching where plasma is non selective about the crystal directions.

For each sample the following cleaning procedure was applied before photolithography as preparation;

- Cutting of the samples 2cm by 2cm in square form which will provide uniformity in photolithography.
- Chemical cleaning steps; (All in semiconductor grade). TCA (Trichlorethan), Acetone, Propanol; All samples were boiled and exposed to vapor cleaning of the above materials in a given sequence. By this sequence each chemical cleans the residue from the former one.
- N<sub>2</sub> gun blowing to dry out after each step.
- Baking at 70–80°C temperature about 20 min in the oven.



**Figure 3.3:** (100) oriented GaAs wafer illustrating cleavage planes and anisotropic as evidenced by a raised mesa and etched slots

Some of the samples were recleaned by wiping with these chemicals if their lithography step failed, and the process was repeated. In a very rare cases ultrasonic cleaning was applied in case of peeling off of the metalization was encountered.

The most important of all in the cleaning process is to follow a continuous process flow (i.e., without giving any long delays between the process steps).

### 3.3 Photolithography

In planar technology complex devices are obtained after successful steps in sequence. The beginning of these steps is covering the substrate by a radiation sensitive material called photo-resist while photolithography is patterning the required model on the photo-resist for subsequent steps. This is achieved by passing high energy radiation or UV-light through a mask containing the pattern and illuminating the photoresist covered substrate.



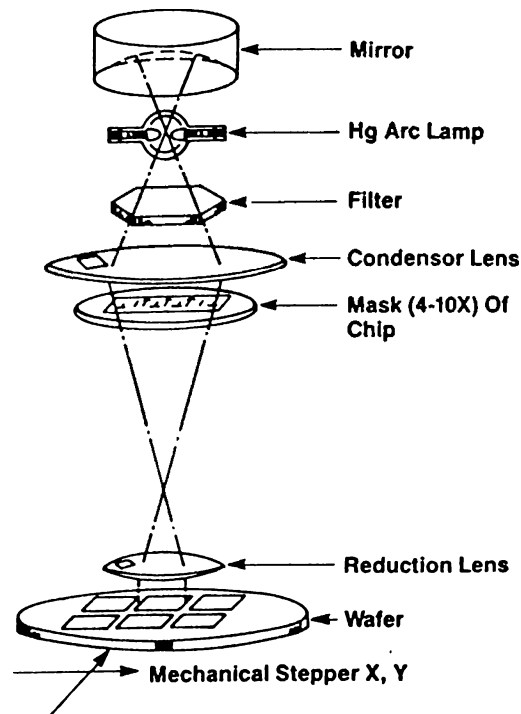


**Figure 3.4:** Schematic of refractive optics reduction projection printer.

Main elements of photolithography can be summarized as follows<sup>44</sup> (figure 3.4).

- Source for exposition.
- Mask containing the required pattern.
- Different lenses and mirrors (Depending on the type of source).
- Mechanical setups for precise aligning and adjustments.
- Photo-resist material.
- Substrate which will be processed.

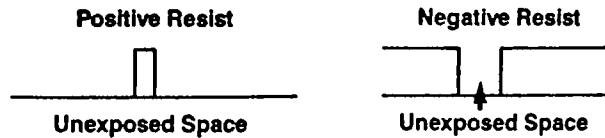


Figure 3.5: Positive and Negative Photoresist behavior after the develop

### 3.3.1 Photoresists

Photo-resists are classified into three different types as; positive photo-resists, negative photoresists and high radiation sensitive e-beam resists. In positive photo-resist applications, photo-resist areas which are exposed to radiation are removed from the substrate by a proper solvent called developer. While the process for the negative photo-resist is reverse of this procedure (figure 3.5).

Both types of photo-resists are suitable for reactive etching processes but only positive photo-resist handles the lift-off applications. Main idea behind the exposition is to change chemical structure of photo-resist material from one form to another (i.e., polar to nonpolar or polymer to monomer). Also by adding different chemicals to photo-resists their capabilities can be adjusted (contrast, speed, sticking coeff. etc.) see table below.

### 3.3.2 Printing

Optical lithography depending on the distance between the mask and the substrate is divided into three types. If the distance is on the order of centimeters, it is called projection printing. For small separations of about few microns, it is called proximity printing and the last one is contact printing where mask touches the substrate.

In projection and proximity printing techniques resolution is weak compared to contact printing, but for repetitive printing (steppers) contact printing can not be used because it is always contiguous for the mask and substrate. For pilot productions contact printing is the most effective one since it gives the best light

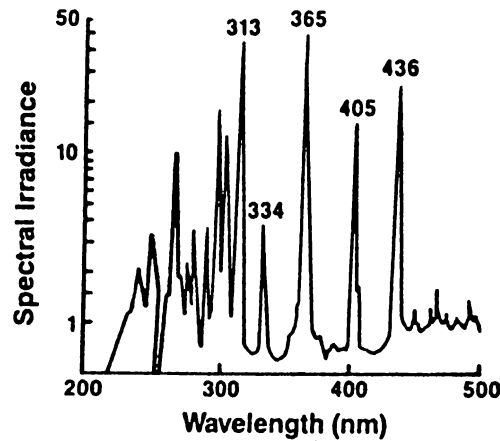


Figure 3.6: Mercury lamp output for resist exposure.

intensity distribution between the mask and the substrate.

With these techniques optical lithography uses different types of exposure sources which emit light in different spectral regions. One of the popular sources of optical lithography is Hg arc lamp and it has emission spectra in several strong lines. Some of the lines are 365 nm (I-line), 405 nm (G-line), 435 nm (G-line) Figure 3.6. Whereas Hg arc lamp has weak emission between 360–450 nm region and is replaced by other optical exposure sources.

### 3.3.3 Experimental

Comparing the cost of optical lithography with other techniques and since the fabrication is just for pilot production, optical exposition technique is preferred for laser diode fabrication. The device chosen for this purpose is a MJB-3 UV-300 mask aligner (figure 3.7) which is equipped with a 300 watt Hg arc lamp and suitable optics for 320 nm wavelength from Karl-Suss. The device is capable of exposing in two different types of printing, contact and proximity with standard and high precision modes. The device was calibrated by a model 1000 UV power-meter on chuck exposition area with  $\pm 5\%$  to continuous intensity mode at  $12.5 \text{ mW/cm}^2$ .

The chosen wavelength is very close to deep UV, because small  $\lambda$  wavelength

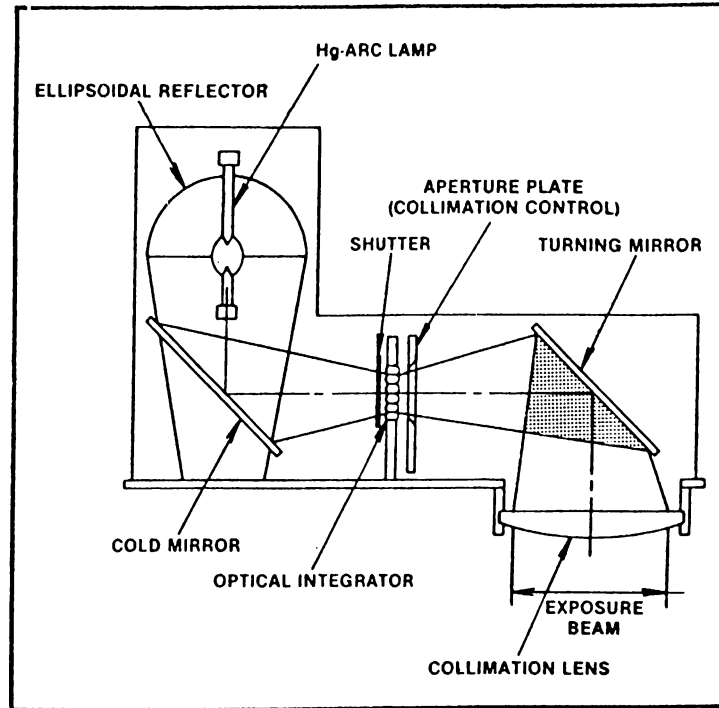


Figure 3.7: Basic schematic of MJB-3 UV-300 Mask Aligner

value offers us contrast enhancing, compensation for standing waves and substrate reflectivity and extending the resolution as wavelength is inversely proportional to the energy of radiation.

Of course one of the main drawbacks of using shorter wavelengths is loss of depth of focus. Numerical aperture of a lens is given by NA,

$$NA = n \sin(\theta) = \frac{D}{2f}$$

$\theta$  (View angle),  $f$  (Focal length), NA (Numerical aperture)

$n$  (index of refraction),  $D$  (lens diameter).

Resolution of a lens at Rayleigh limit for two opaque objects ;

$$W = \frac{k\lambda}{NA}$$

$\lambda$  (wavelength),  $k$  (material constant<sup>45</sup>) values are given in the table below.

$k = 0.3$	top surface image resists
0.5	multilayer resists
0.75	single layer resists
1.1	resists over reflective surfaces ( Al, Au)

Depth of focus (DF) of a lens for a determined wavelength  $\lambda$ ;

$$DF = \pm \frac{\lambda}{2NA^2}$$

Because of the self aligning nature of the fabrication of laser structures in IAL laboratories only one lithography step was applied in the whole process. Photoresist AZ 5214-E with AZ 400K developer were chosen for later lift-off applications.

For spinning of the photo-resists, Model SM 120 spinner which is equipped with a photo-resist dispenser unit was used. Device is capable of blowing  $N_2$  before dispensing the photo-resist for final cleaning and has various speeds between 500–10.000 rpm and acceleration controls for two different settings. In baking steps temperature controlled Heraeus–6030 oven was used.

The following lithography steps are applied during fabrication after cleaning of the samples,

- Spinner Part :
- Dispensing of the HMDS.
- Spinning at speed 1. 1000 rpm of 2 sec.
- Spinning at speed 2. 5000 rpm of 10 sec.
- Coating of photo-resist :

- Filtering photo-resist at low pressures up to  $0.2\mu\text{m}$ .
- Dispensing of the photo-resist.
- Spinning at 1000 rpm. of about 10 sec.
- Spinning at 5000 rpm. of about 40 sec.
  
- 1cm Prebaking at 85 C about 40 min in oven.
  
- Aligning and Masking :
  - Mask containing  $5\mu\text{m}$  and  $12\mu\text{m}$  stripes with separation of  $600\mu\text{m}$  is used.
  - Samples are aligned along the major axis and exposed at Cl2 mode:  $12\text{ mW/cm}^2$  for 38 seconds.
  
- Developing :
  - Exposed samples are developed in AZ-400K + DI water solution (1:4) in contrast mode of developing. Developing was done in a dynamical way in a stirrer along the stripes.
  - After developing, samples are rinsed in continuous flow of DI water.
  - Dry filtered  $\text{N}_2$  spraying.

### 3.3.4 Process notes

Reproduction of the image is influenced by many factors such as film thickness, prebake conditions, exposure conditions, developer parameters (i.e., concentration, agitation, temperature, developing time), surface topography and image geometries. Applying agitation which is known as dynamical developing, increasing temperature, and increasing developing time yields big amounts of film losses from the surface in short times. What is required in our process was controlling the contrast of the photo-resist and obtaining the highest possible contrast in the stripe figures. In case of over-exposition and over developing for positive photoresist applications loss of photo-resist from the patterned figures is intolerable for the following dry etch steps. Above process steps are the optimum ones giving the best results.

Before application of photo-resist using one of the surface primers HMDS (Hexamethyldisilazane) is found to be beneficial. Application was done in pure form where also diluted and vapor phase applications are taking place in lithography. To achieve proper adhesion properties, it is necessary for the resist and the substrate to have equal surface energy values. The surface energy of water is 72 dyne/cm<sup>2</sup>, the approximate energy value of photo-resist is 32–35 dyne/cm<sup>2</sup> and surface energy of an HMDS treated surface<sup>46</sup> is 4.6–16 dyne/cm<sup>2</sup>. Since HMDS is hydrophylic in nature, resist must be applied immediately afterwards onto the treated surface. Vacuum is best for this purpose. Removing water from the surface by dehydration is also very important. When no HMDS is used a physisorption condition exists. In case of long delays between dehydration and resist applications lifting of the photoresist in further steps can be seen. With priming agent aging is also seen by chemically adsorption of water (chemisorption) but it is much more slower.

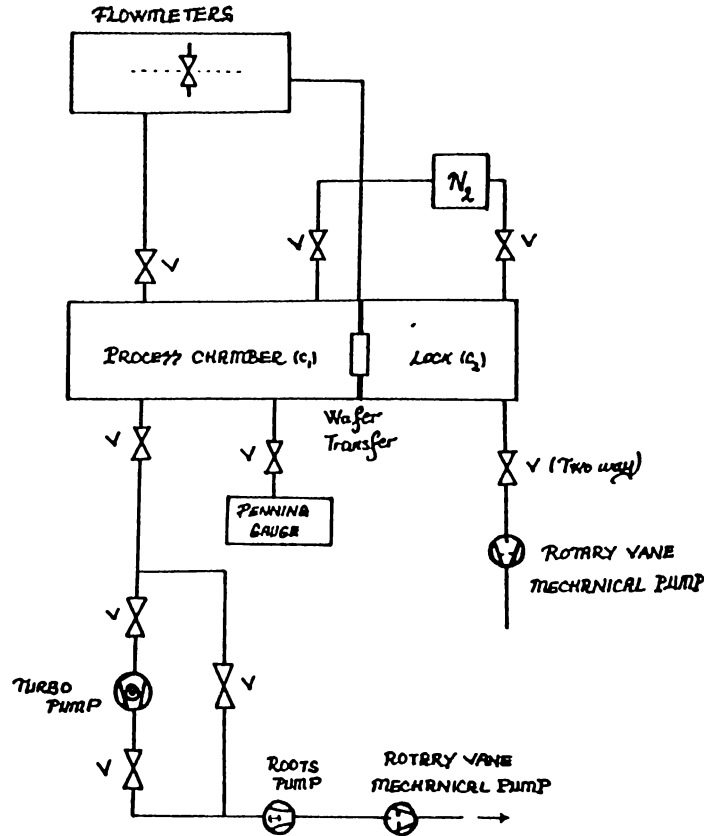


Figure 3.8: Basic schematic of RIE

### 3.4 Reactive Ion Etching (RIE)

Asymmetric parallel reactor usage at low pressures in plasma etching is usually called as reactive ion etching (RIE). The term "diode reactor" has also been used to refer to reactors of such kind. Before giving the detailed information on RIE, mechanism of plasma etching may be helpful. A simple plasma reactor consists of opposing parallel plate electrodes in a chamber that can be maintained at low pressure, ranging from 0.01 to 1 Torr figure 3.8. When a high-frequency voltage is applied between the electrodes, current flows through the gas mixture, forming a plasma that emits a characteristic glow. Light emitted at this moment is the characteristic of plasma and material inside. It can be used in *in-situ* monitoring processes.



Neutral and charged species exposes the material at the lower electrode surface. Some of these species react with the substrate and form volatile products which evaporate hence etching the substrate. In such plasmas ionization rates are very small; one charged particle per neutral atom and molecule densities leading to  $10^9$ – $10^{11}$  cm<sup>-3</sup>. Positive charge is mostly singly ionized atoms and negative are the free electrons. Main carriers are the electrons since they are light and mobile. Neutral gas remains at normal temperatures while electrons gain tens of thousands of Kelvin from the applied field. Because electron mass is almost 0.0005 times that of other species, main contribution of cooling the plasma comes from the heat transfer between the plasma gas and the chamber walls. Elevated electron temperature permits electron molecule collisions to excite high-temperature reactions that form free radicals.

Plasma etching is characterized according to rate, anisotropy, selectivity, the degree of loading effect and texture (surface roughness) on the surface of the samples.

By convention, the term anisotropic etching refers to preferential erosion in a direction normal to the surface of the wafer. Selectivity is the ratio of etching rates between two different materials immersed in the same plasma, for example, GaAs and Al<sub>x</sub>Ga<sub>1-x</sub>As. Loading is a term used to describe a measurable depletion of active etchant species from the gas phase brought about by the consumption of this reactant in the etching process.

In principle the plasma etchant feed gas is chosen with required selectivity over processed materials and minimization of any loading effect and to avoid excessive surface texturing and polymer deposition. Anisotropy degree becomes important in etching of 3–5 μm patterns. Some of the etching profiles are given in (figure 3.9).

Isotropic etching has no preferential direction. This leads to isotropic circular profiles which undercut a mask. Overetching increases the undercut and radius eventually making sidewalls nearly vertical. In anisotropic etching, the sheath field makes ions strike horizontally and ion assisted chemistry forms profiles with vertical sidewalls that line-up with the edges of the mask. Anisotropy is

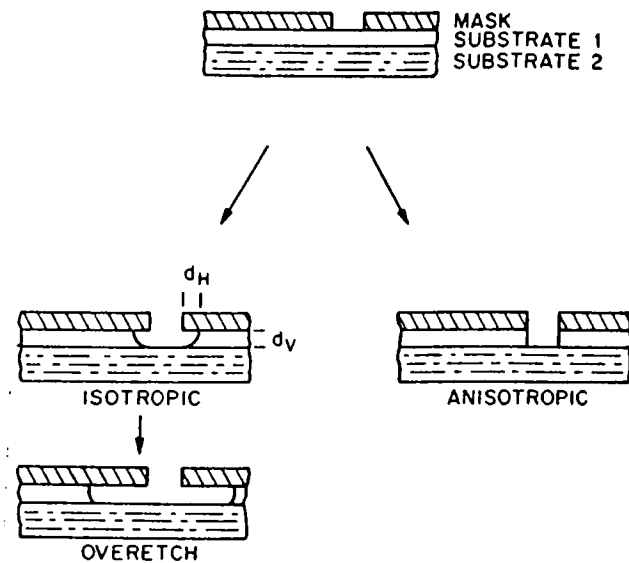


**Figure 3.9:** Isotropic(left) and anisotropic etching(right)

useful to get fine figures in micron range. While isotropy is helpful for stripping of photoresist, etching large figures and removing of oxidation masks in an economical way. Isotropic etchants often exhibit a loading effect that results from etchant depletion in the gas phase caused by reaction with the substrate material. If a significant portion of the reactive etchant species is consumed in etching reactions, their concentration will decrease rapidly with the area of etchable material in the reactor. Use of a large reactor volume with high surface area will minimize the sensitivity of etch-rate to the area of etchable material. If more than one species participate in etching, like in fluorine based plasmas where Cl and F atoms individually helps etching, each shows its own loading effect. Concentration of fluorine atoms etching GaAs in a plasma is usually limited by reaction with substrate, giving loading effect. Chlorine atom concentrations in chlorine containing plasmas tend to recombine rather than etching reaction. Chlorine plasmas is commonly insensitive to load size and feature topology and ion bombardment determine the etching rate and nature. One can use them as a good drilling machine in micro-fabrication applications.

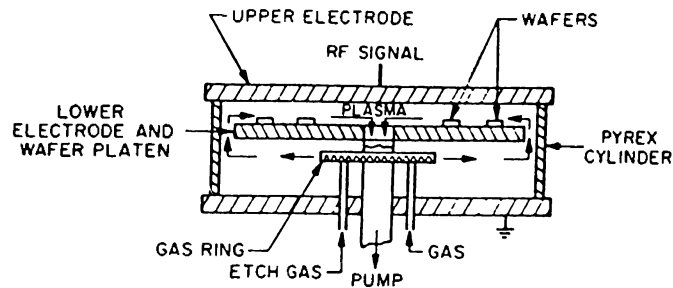
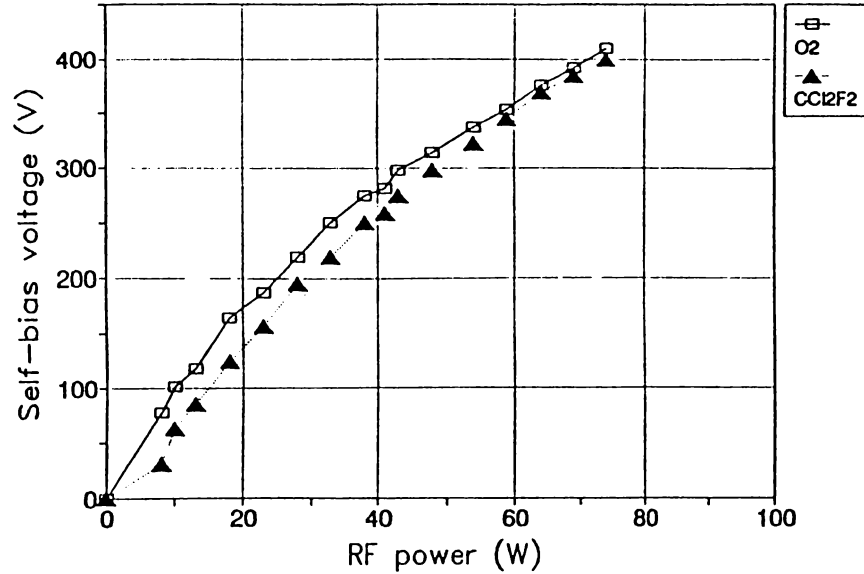


Figure 3.10: A parallel-plate "Reinberg" style reactor with radial gas flow.

In RIE reactors, wafers are placed on the smaller bottom electrode. Parallel plates are highly asymmetric and the external circuit has a blocking capacitor so that smaller electrode develops a negative D.C. bias superimposed on the applied RF signal (figure 3.10).

The high potential RF power lead is usually connected to smaller electrode, with the larger electrode grounded at common potential. This is necessary to maintain a large area ratio since there are usually grounded surfaces elsewhere, in and out of the reactor chamber. These areas are capacitively coupled to the plasma and therefore increase the effective area of grounded electrode. In controlling the etching, instrumental parameters or discharge variables are used instead of theoretical models. Among them radio frequency(RF) input power, reactor pressure, RF excitation frequency, temperature, flow rate, feed gas composition, reactor geometry and material of construction have the great importance. Choosing one of these parameters and fixing the others is the way to study the effect of over etching.

Pressure directly influences major phenomena that control plasma etching. As pressure is lowered below about 0.1 torr the characteristic potentials across the sheaths and voltage applied to a discharge rise sharply in the range of hundred volts to 1000 volts. As this happens mean free paths of the species also increase so the larger sheath potential induces a corresponding increase in the energy of ions bombarding substrate surfaces. Sputtering doesn't take place until ion



**Figure 3.11:** Dependence of  $U_{sb}$  on RF power (RIE) for  $O_2$  and  $CCl_2F_2$ ;  $P=0.8$  Pa

bombardment energy exceeds a material and ion specific threshold.<sup>47</sup> Sputtering efficiency is defined as atoms removed per incident ion and this increases beyond threshold and usually stays well below unity. Since low pressure favors higher ion bombardment energies it also favors etching by the energy driven damage mechanisms. However ion energies far above the threshold are undesirable because selectivity ratios decrease with increasing ion energy and because there may be induced damages to devices.

$CCl_2F_2$  is a well known selective etchant of GaAs on  $Al_xGa_{1-x}As$ . Because of this reason it is used for fabrication of modulation doped FET's and other heterojunction devices. During the etching of GaAs, volatile  $AsF_xCl_y$  and  $GaCl_x$  products are formed until a barrier layer is created when the GaAs/ $Al_xGa_{1-x}As$  interface is reached. The barrier layer consists of  $AlF_3$  and  $GaCl_xF_y$ . This surface layer prevents the etching of aluminum alloys at intermediate pressures (30 mtorrs).  $CCl_2F_2$  selectively etches GaAs up to 1000 times faster than  $Al_xGa_{1-x}As$ . Unsaturated  $CCl_xF_y$  species can form thin side-wall films, which simulate anisotropic etching by ion bombardment.

In RIE at low pressures (few mtorrs) at high self bias (SB) voltages GaAs in  $\text{CCl}_2\text{F}_2$  shows acceptable anisotropy and etching-rate. At high pressure the unsaturated species can be adsorbed at the surface and polymerize (forming thick polymer film). The growth of the polymer film increases with partial pressure of the unsaturated  $\text{CCl}_x\text{F}_y$  species. This polymer formation completely stops the etching (mostly in  $\text{Al}_x\text{Ga}_{1-x}\text{As}$  etching galliumtrifluoride is dominant and involatile).

In laser diode structures, to etch ridge-waveguides freon-12 ( $\text{CCl}_2\text{F}_2$ ) was chosen as process gas. Machine used for this purpose is a parallel plate Leybold LE-301 reactive ion etcher operating at 13.56 MHz RF voltage. Chamber pressure can be lowered by turbo pumping down to few millibars. Water cooled lower electrode gives the ability to suppress the thermally activated reactions. By this means only energy driven, ion assisted etching reactions, that give anisotropic profiles, can occur. Choosing pressure at 0.4 Pa gave us decrease of selectivity between one third, to one fourth. Self bias voltage was seen around 350 V with 54 W actual RF power (figure 3.11). In GRINSCH structure material thickness that must be etched was calculated as  $0.7\mu\text{m}$  in capping layers. Etching was stopped  $0.4\mu\text{m}$  away from the layers where grading begins. Taking into account that anodic oxide will also consume from the surface about  $0.1\mu\text{m}$ , stopping  $0.4\mu\text{m}$  away from graded layers helps the confinement of lateral modes inside the waveguide. Etching was performed at two steps. In the first step, sample was etched up to  $5200\text{ \AA}$  from the surface with the parameters:

First Step:

Etching gas :  $\text{CCl}_2\text{F}_2$  ( Freon 12 )

Flow : 4 sccm.

Pressure : 0.4 Pa

Power RF : 46 W ( at 13.56 MHz.)

Self bias voltage : 322 Volts

Etching time : 42 min.

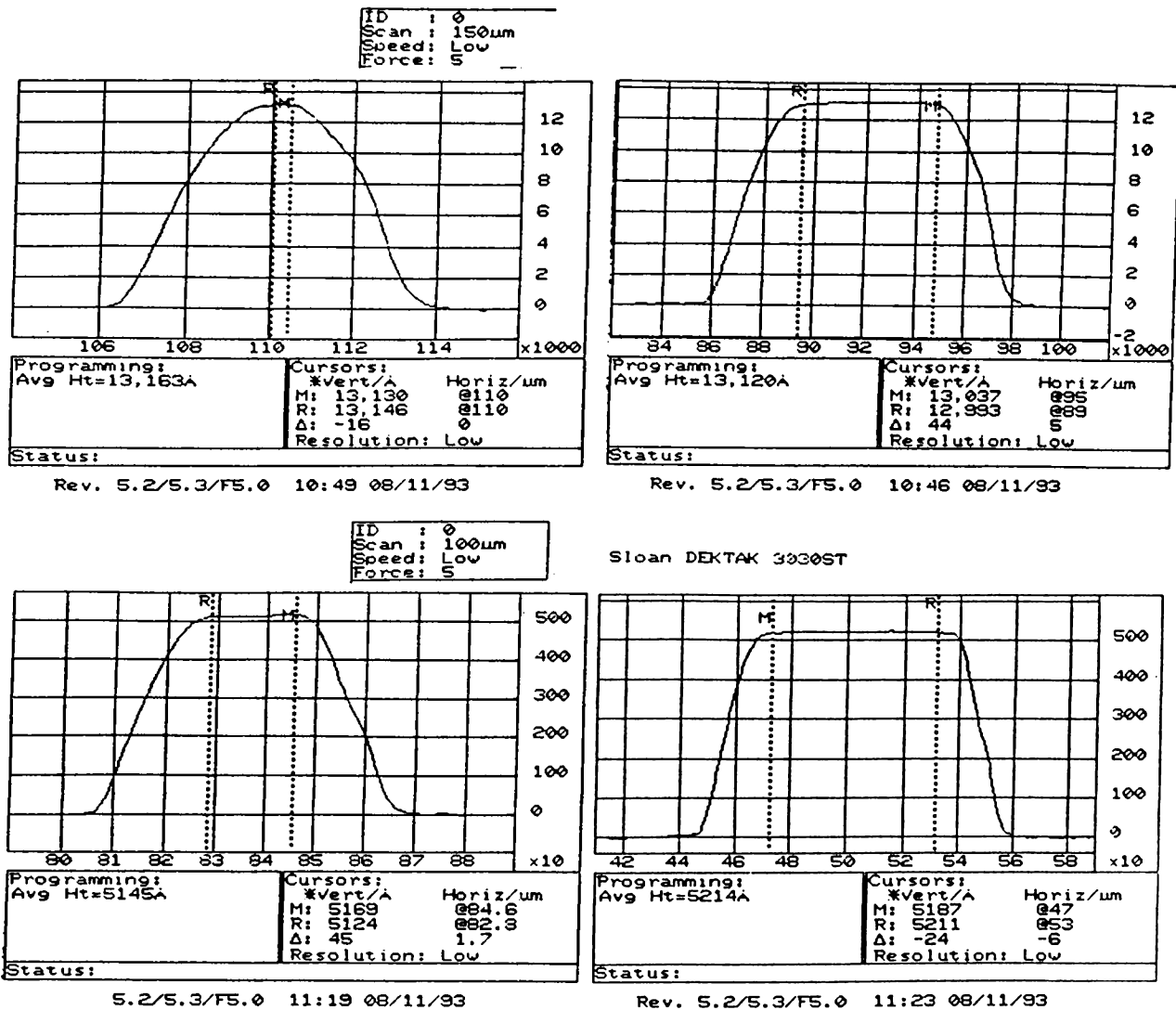


**Figure 3.12:** Profiles of the 5μm and 12μm stripes: (a) Before etching (b) After first etching step.

Dummy samples run in the same process was taken out and after stripping of the photoresist, etch rate was calculated from the DekTak stylus profilometer reading, (figure 3.12).

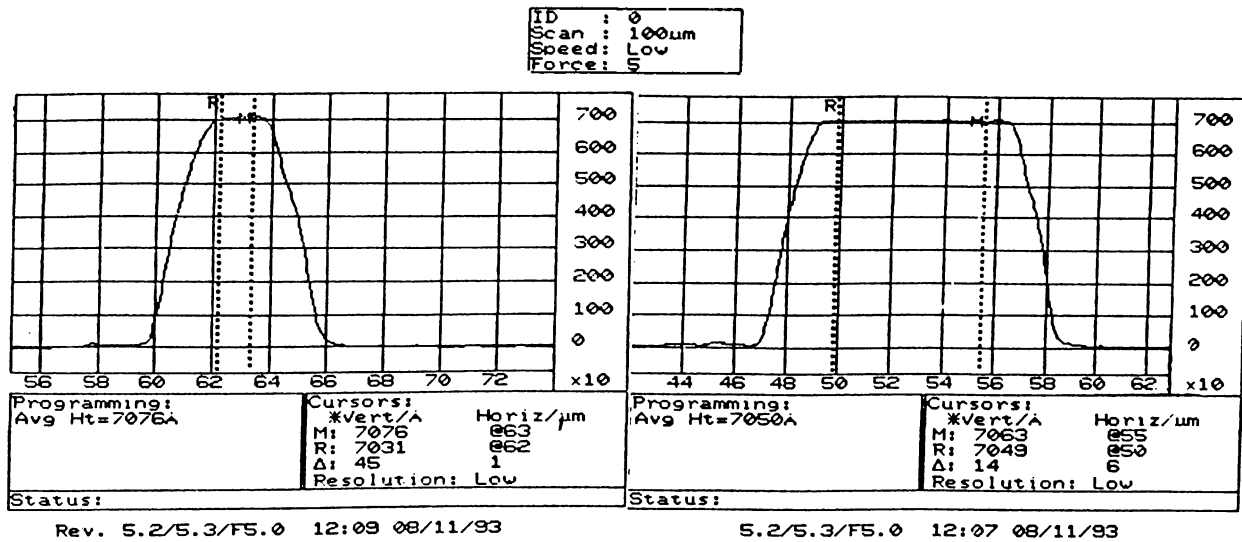


**Figure 3.13:** Etching profiles of the 5μm and 12μm stripes after second etching step.

Depending on the data obtained from the first step second etching step was performed and same Dektak measurement was done on the dummy sample. After second run, etching depth reached around 7050 Å which is exactly the required etching thickness, (figure 3.13). Second Step :

Etching gas :  $\text{CCl}_2\text{F}_2$  ( Freon 12 )

Gas Flow : 4 sccm.

Pressure : 0.4 Pa

Power RF : 46 W (at 13.56 MHz.)

Self bias voltage : 345 Volts

Etching time : 5 min.  $\text{Cl}_2/\text{BCl}_3$  gas mixtures can also be used instead of the

$\text{CCl}_2\text{F}_2$  plasma. Since this gas mixture doesn't show any selectivity (1:1) between  $\text{Al}_x\text{Ga}_{1-x}\text{As}$  and GaAs and etches them at high rates, up to 4500 (Å)/min ( $U_{sb}=200$  V,  $P=0.8$  Pa, Flow=6 sccm) which lowers the process times. Previous studies<sup>48</sup> of GaAs RIE in  $\text{Cl}_2$  and  $\text{BCl}_3$  plasma was showing 1.5 times less damage

on surface of GaAs in Raman scattering spectrum. Of course small surface damages on GaAs or  $\text{Al}_x\text{Ga}_{1-x}\text{As}$  can somehow be healed in further annealings at metalization step.

### 3.5 Anodic Oxidation

In stripe geometry laser diode devices, to decrease the injected current and to restrict it into a region one must insulate all the areas, except the current path on top of the stripe. There are several ways to achieve this. One of them, possibly the easiest, is to apply anodic oxidation to the *p*-type region.

In our lasers we also chose anodic oxidation. Nature of our process yields self aligning of anodic oxidation area along the stripe, since only the areas that could pass the current through solution are oxidized. Laser structures in the stripe-up position was used as anode and Pt was used as cathode. Cathode Pt was dipped into the anodic oxidation solution while laser structure was held by soft vacuum and placed in touching position to the surface of the solution figure 3.14. After aligning the cathode and anode positions 100 V D.C. was applied to the structure until current dropped to zero. This is the result of self stopping nature of the anodic oxide growth. For successive applications, anodic oxide growth rate for different structures was found as 21 Å per volt in this solution. Applying 100 volts gives us approximately 0.2 μm anodic oxide thickness, dark blue going to purple in color due to interference.

Anodic oxidation solution:

At the first stage 3 gr Citric Acid was mixed with 97 ml DI water. In this way liquid citric acid solution was obtained. This solution is further mixed by 194 ml Etylen Glycol.  $\text{NH}_4\text{OH}$  was added to obtain the final solution until its PH value reads 6.5.



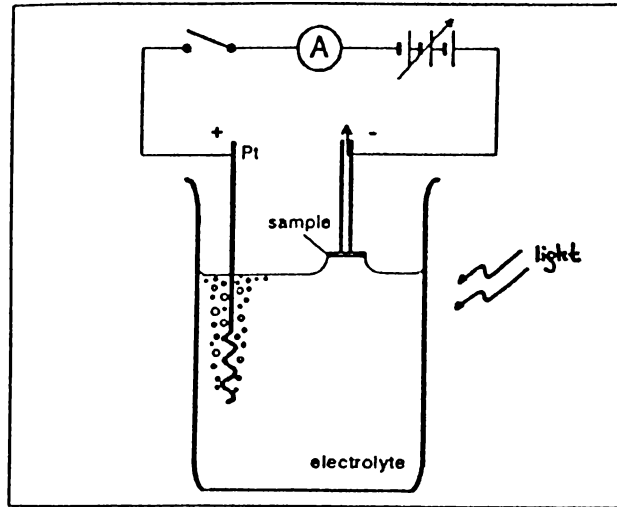
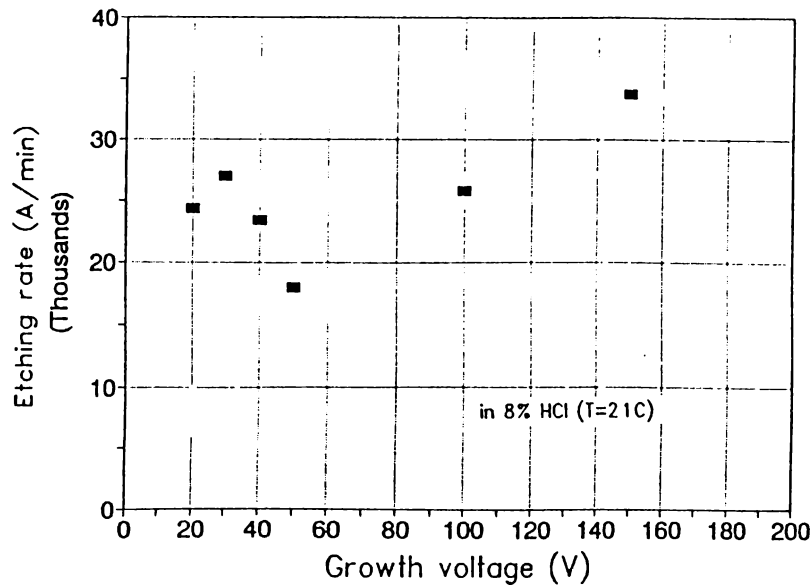


Figure 3.14: Anodic oxidation setup.

### 3.5.1 Process notes

Before anodic oxidation was applied, samples were dipped into the dilute HCl (6–8 %) solution a few seconds. Since HCl is one of the etchants of the GaAs and  $\text{Al}_x\text{Ga}_{1-x}\text{As}$ , it helps to get more smooth and clean surfaces, it is essential for anodic oxide sticking. This way of cleaning is not advised for high Al concentration layers since  $\text{Al}_x\text{Ga}_{1-x}\text{As}$  etching rate is higher than the GaAs in HCl. It may give nonuniform surfaces at the end of acid application. Similar behaviour were observed in the anodic oxidation process for high Al concentration structures. If applied current is set above few tens of a mA even though the oxidation ends fast, some of the areas were found not to be oxidized, while some oxidations areas goes deeper in such structures. In extreme cases these deeply oxidized areas may combine and can penetrate to the stripe, resulting in a loosening of the chip (figure 3.15).

In all of the applications when oxide is grown on the surface of the chip, it was taken out from the solution and dipped and washed in DI water to get rid of any kind of oxidation solution. Following this step chips were dried by dry- $\text{N}_2$  spray and baked at  $55^\circ\text{C}$  about 3 minutes. Putting the chip just at the surface of oxidation solution is essential since any wetting will result oxidation



**Figure 3.15:** Oxide etching characteristic of HCL

of the n-side which is intolerable. Chemical reaction is sensitive to heat and agitation. Agitation mechanically may cause stripping the oxide from some areas while exposition to high intensity light speeds up the oxidation. All the laser structures were excited by light during the anodic oxidation step.

For cases where anodic oxide grew nonuniformly, etching half the thickness of the oxide by the above cleaning method in dilute HCl and regrowing it to again up to  $0.2\mu\text{m}$  can be proposed (figure 3.15). Like in all oxidation processes anodic oxide also grows into the material and the thing that must be taken into account here is to allow enough thickness of capping layers for this extra step in RIE.

GaAs native oxide which is mainly composed of gallium-trioxide and arsenic-trioxide is known to be an unstable oxide. Because of this deficiency it can not insulate the laser structures at high current pumping rates (giving high leakage currents) putting another insulating layer (noncrystalline  $\text{SiO}_x$ ) by PECVD was found beneficial.

### 3.6 PECVD and Lift off of SiO<sub>2</sub>

As is known silicondioxide (SiO<sub>2</sub>) and silicon nitride (Si<sub>3</sub>N<sub>4</sub>) is widely used in contemporary photonics and semiconductor industry. In integrated circuit applications, SiO<sub>2</sub> and Si<sub>3</sub>N<sub>4</sub> can be deposited onto surfaces in different ways. Thermal oxidation of Si to obtain SiO<sub>2</sub> films gives especially good results as indicated by a refractive index of  $n=1.45$ . However, during thermal oxidation extremely high temperature of the chamber,  $T_c \geq 700^\circ\text{C}$ , may destroy many of the parameters of structures such as ohmic contacts and doping profiles.<sup>49</sup>

Among many methods, Plasma Enhanced Chemical Vapor Deposition (PECVD) is widely used since it enables low temperatures of deposition, controllable index of refraction and film stress, as well as uniform film thickness and properties.<sup>50</sup>

- With low temperature of deposition, dopant redistribution minimization and protection of sensitive substrates can be achieved.
- With controllable refractive index, anti reflection coatings are achievable and dielectric constant can be controlled.
- With controllable film stress, cracking can be avoided and adhesion can be promoted.
- With controllable film thickness and properties, high yield manufacturing compatibility with the following process steps, are achieved.

In PECVD, to obtain a uniform and a good quality SiO<sub>x</sub> films and to use them as a fabrication step in ridge-waveguide laser diodes was aimed. The machine used for this purpose was a Plasma Technologies  $\mu\text{p-Dp80}$ , a computer controlled, parallel plate plasma reactor with cathode diameter of 24 cm which is arranged in plasma deposition configuration with cathode and anode separation 20 mm (figure 3.16). Since local temperature at the samples which are put onto the lower electrode is an important parameter, to achieve uniform depositions,

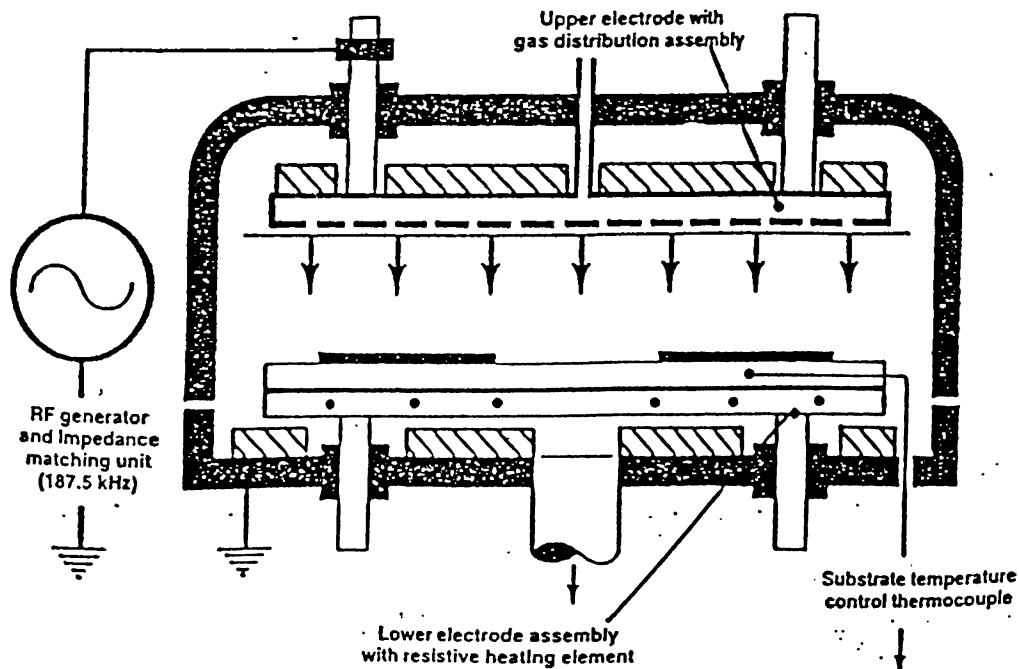
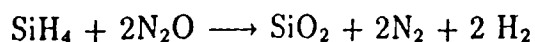


**Figure 3.16:** Parallel plate  $\mu\text{p-Dp80}$  plasma reactor in PECVD configuration

lower electrode is normally chosen as the larger one, supplying the required heat capacity.

Process gases were selected as nitrogen balanced silane ( $\text{SiH}_4 + 98\% \text{N}_2$ ) where  $\text{N}_2$  was used as a carrier gas and dilution gas to obtain safe working conditions and nitrous oxide ( $\text{N}_2\text{O}$ ) with the flow ratios of (180:720) sscm respectively. In each run different combinations of cathode temperatures ( $250^\circ\text{C}$ ,  $100^\circ\text{C}$ ) with different RF powers (7 W and 18 W actual at 13.56 MHz RF frequency) and reactor pressures (0.4 to 1.8 Torr) were tried with rough pumping. At low temperatures and low pressures, strikes in plasma reactor are used to initiate the plasma. Samples are cut into 1.5 cm to 1.5 cm as squares and each positioned at the center of lower electrode to obtain uniform film thicknesses.

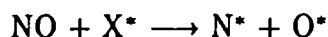
Chemical reaction for silane and nitrous oxide mixture under RF excitation is basically as follows:



Studies by Longeway *et al.*,<sup>51</sup> and Remote PECVD studies<sup>52,53</sup> indicate that gas phase precursor formation and surface chemistry plays an important role in deposition. The precursor molecule for oxide formation is given as disiloxane  $(\text{SiH}_3)_2\text{O}$ . In the RPECVD studies it was indicated that this molecule is present in the surface reaction at the substrate, where hydrogen is replaced by oxygen. This surface reaction yields near-stoichiometric  $\text{SiO}_2$ . In diluted silane plasma, carrier gas helps to production of disiloxane and promotes the SiH and SiO bonds changing in surface reaction. Dilution gas also reduces the rate of impurity bondings such as SiN. Typical surface reaction sequence for this case is:



and



$\text{X}^*$  is either excited carrier gas atoms or electrons. Carrier gas atoms also prevent the recombination of the excited oxygen atoms. Excited oxygen atoms react with the  $\text{SiH}_4$  to produce siloxane and participate in the  $\text{SiO}_x$  formation.

The PECVD films have little short-range structural ordering. Chemical bonding within the film may vary. The plasma assisted deposition process sometimes has been called plasma polymerization to emphasize that film may be randomly bonded, highly cross linked and of variable composition. Therefore chemical species other than the required ones may be included in the film. In this sense we can say that plasma-assisted deposition is much more complicated than the plasma-assisted etching in which final products are pumped out from the chamber. In films, a range of stoichiometry is possible, depending on the plasma and operating parameters. This variation in stoichiometry gives us the ability to adjust the physical and electrical properties.

In order to characterize the PECVD process of  $\text{SiO}_x$  a number of PECVD films were grown on Si substrates. These films were evaluated both by Fourier Transform Infrared Spectroscopy and ellipsometry. In measurements of refractive

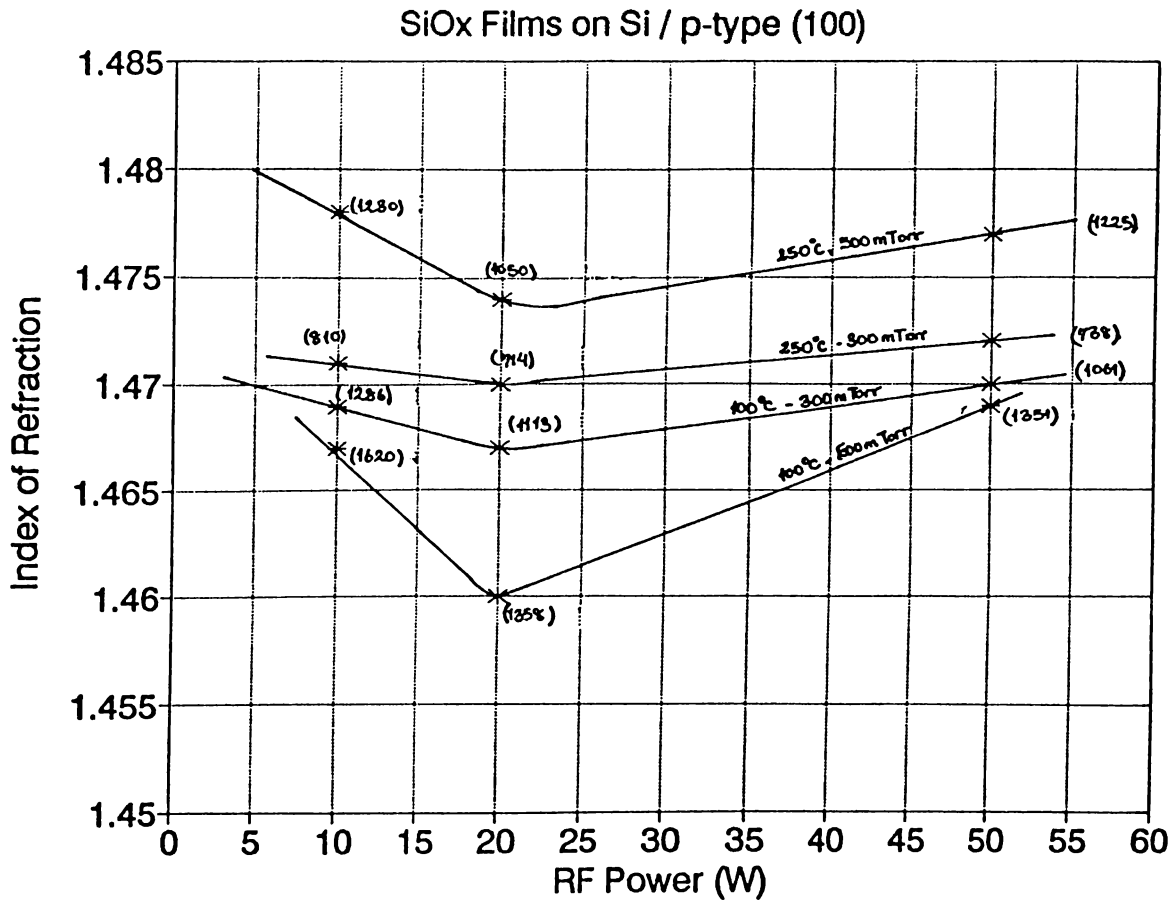


**Figure 3.17:** SiO<sub>x</sub> Films on Si *p*-type (100). Data in parenthesis indicate the thickness of the film in Å

index and thickness of the films an ellipsometer with He-Ne laser at 6263 Å along with polarizer analyzer combination at room temperature was used. A summary of index of refraction and thickness measurements is given in figure 3.17.

Here we first plot index of refraction as a function of RF power.<sup>61</sup> The data points form a family of curves with chamber pressure and temperature as variables. The lines are drawn to guide the eye and are not a fit to data. It is clear data as substrate temperature goes up the index of refraction increases to an average value of 1.476. For lower temperatures the index of refraction drops. At 100°C and a chamber pressure of 300 mTorr average values of the index of refraction is about 1.469. While the difference is not insignificant the advantages

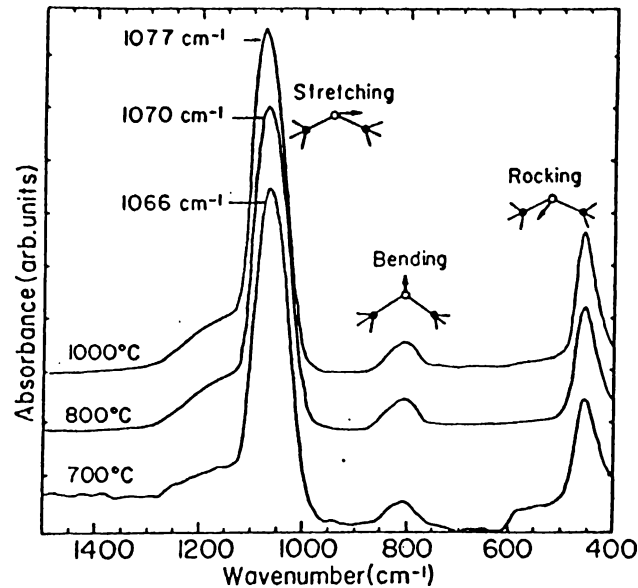


**Figure 3.18:** IR absorption spectra for thermally grown films at 1 atm of dry oxygen at temperatures of 700, 800 and 1000°C. O atom motion for rocking, bending and stretching vibrations are also indicated

of processing brought about by lower temperatures outweighs this small drop in the index of refraction. Due to low temperature of growth the  $\text{SiO}_x$  films grown on GaAs substrates are expected to have similar properties.

Absorption spectroscopy can be used to determine both composition and quality of silicon oxides.

Thermally grown stoichiometric  $\text{SiO}_2$  shows us the following peaks in the normalized IR absorption spectra (figure 3.18) with the three vibrational modes which correspond to rocking, bending and stretching motions of the oxygen atoms. Motions of the atoms are given basically by choosing the plane of the Si-O-Si bond as a reference coordinate system.<sup>57</sup>

Films which are grown by PECVD directly from  $\text{SiH}_4$  and  $\text{N}_2\text{O}$  gas mixtures have IR absorption peaks corresponding to SiN, NH, SiH and OH bondings in addition to the above three Si-O-Si vibrations. S-OH  $3660\text{ cm}^{-1}$ , Si-H  $2250\text{ cm}^{-1}$ , N-H  $3400\text{ cm}^{-1}$ , H-OH  $630\text{ cm}^{-1}$  give the corresponding peak positions. As it

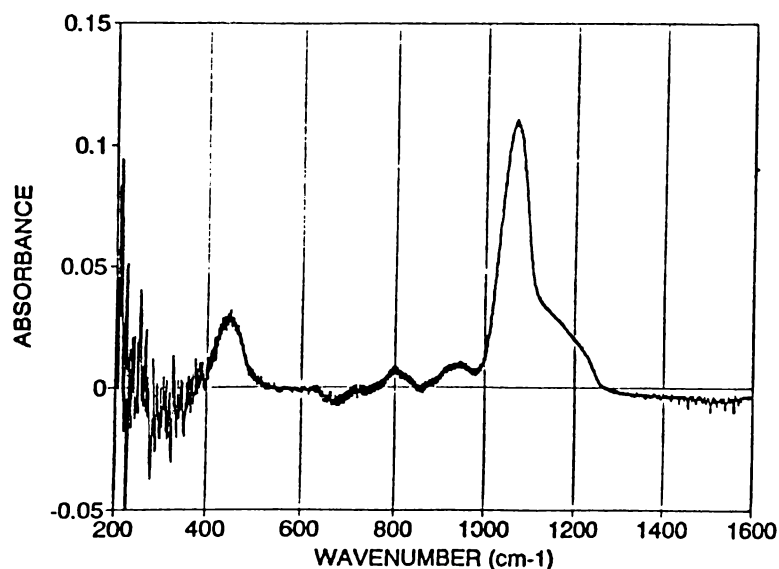


Figure 3.19:  $\text{SiO}_x$ -24 absorption spectra

is shown in several studies<sup>58,59</sup> the frequency and the width of the stretching vibrations are sensitive to the stoichiometry of the deposited film. This peak also indicates the densification due to internal compressive stress or film involving the nitrogen bonding groups.

In order to determine the composition and quality of PECVD deposited  $\text{SiO}_x$  films absorption spectroscopy was carried out. For the series of films absorbance were recorded over a wide range of 200 to 6000  $\text{cm}^{-1}$  with 2  $\text{cm}^{-1}$  resolution at room temperature. Figure 3.19 shows a typical IR absorbance for the films deposited at 100°C, 300 mTorr chamber pressure, and at 10 W RF power. This film shows the three main IR absorption peak of the  $\text{SiO}_2$ ; a stretching vibration at 1068  $\text{cm}^{-1}$ , a bending vibration at 941  $\text{cm}^{-1}$ , rocking vibration at 450  $\text{cm}^{-1}$ . No absorption peaks corresponding to SiOH and SiH groups were observed. Also no water was observed in the grown film. Small peak observed at around 3380  $\text{cm}^{-1}$  corresponding to SiNH bonding groups disappeared after annealing at 770°C in  $\text{Ar}_2$  atmosphere. Our film has the  $\text{Si}_{1.9}$  ( $x \sim 1.9$  giving 1068  $\text{cm}^{-1}$ )



stoichiometry<sup>59</sup> with small compressive stress. We observed that if the time is increased in annealings, stretching mode shifts to higher frequencies indicating that the film shifts to better stoichiometry. Critical annealing time to reach  $1075 \text{ cm}^{-1}$  seems to be 5 min at  $770^\circ\text{C}$  temperature. Full width at the half maximum value for this mode went down from  $78 \text{ cm}^{-1}$  to  $55 \text{ cm}^{-1}$  upon annealing. This sharpening in the peak position indicates increase of ordering in the structure of the film.

A summary of processing conditions and stretching vibration peak frequency ( $\nu$ ), FWHM of this peak ( $\Delta\nu$ ) and the intensity ratio of high frequency shoulder ( $1150 \text{ cm}^{-1}$ ) to peak intensity as  $R$ , is given in the table below.

Growth Temp.		250°		100°	
Chamber Press.		500 mTorr	300 mTorr	500 mTorr	300 mTorr
$P_{RF}=10\text{W}$	$\nu \text{ cm}^{-1}$	1059	1060	1069	1068
	$\Delta\nu \text{ cm}^{-1}$	85	78.6	71	81
	$R$	0.27	0.256	0.30	0.29
$P_{RF}=20\text{W}$	$\nu \text{ cm}^{-1}$	1059	1058	1066	1068
	$\Delta\nu \text{ cm}^{-1}$	78.6	75	71	74.6
	$R$	0.25	0.24	0.287	0.31
$P_{RF}=30\text{W}$	$\nu \text{ cm}^{-1}$	1055	1054	1064.5	1064
	$\Delta\nu \text{ cm}^{-1}$	85.7	78.6	75	78.6
	$R$	0.315	0.24	0.299	0.32

As is seen from the table as the RF power increases the peak position goes to lower wavenumbers. Higher RF power result also in higher deposition rates. This implies that higher RF power results in denser films which should show higher peak positions. The apparent contrast with our data is solved by the introduction of a model where some fraction of the film contain micropores which reduces the effective density of the films.<sup>60</sup>

At low substrate temperatures these micropores regions play the role of

decreasing the density as growth rate is increased by increase in pressure. Their behavior depend on the temperature of deposition and normal densification takes place as temperature of the deposition is increased and microdensification seems to be dominant only at low temperature regime. Increasing the deposition temperature can be thought as a soft annealing. From a series of depositions we select the one which is grown at 100°C cathode temperature,  $P=0.3$  torr chamber pressure and 10W RF power. These deposited films gave us controllable low chemical etching rate in HF (1:6) changing in the range from 19.2 Å/sec to 41.6 Å/sec and reasonable index of refraction of  $n=1.469$ . Stretching mode peak of these films were 1068  $\text{cm}^{-1}$ .

After applying photolithography on the samples with the mask containing the 5 $\mu\text{m}$  and 12 $\mu\text{m}$  laser stripes, each sample was etched in buffered hydrofluoric acid solution (HF 1:6) until the substrate was reached. From the etching times and the height of photoresist covered  $\text{SiO}_x$  stripes, as measured by DekTak stylus profilometer after removing the photoresist in hot acetone, deposition and etching rates were obtained using ellipsometry. From the above calculations growth rate was obtained for different substrate temperatures at different pressure and RF power values (figure 3.20). Since we can adjust pressure, as pressure is increased, growth rate increases. This means that we are not in the pressure regime where mean free path of the species decreases to a limit which they can not gain enough energy from the field resulting a decrease in growth rate. As RF power is increased, growth rate is also increased since ionization rate of the gas molecules increases.

This recipe was applied in quantum well laser diodes as a fabrication step after obtaining the GaAs native oxide. A rich PECVD grown good  $\text{SiO}_x$  provides a second 1000 Å isolation layer in addition to native oxide. Because of the low temperature of this step, there was no difficulty in lifting off the  $\text{SiO}_x$  from the 5 $\mu\text{m}$  and 12 $\mu\text{m}$  stripe areas in hot acetone bath. To understand the ability of  $\text{SiO}_x$ -lift off for low temperatures in different geometries, processes were tried with different geometries and it was found that good results can be obtained in

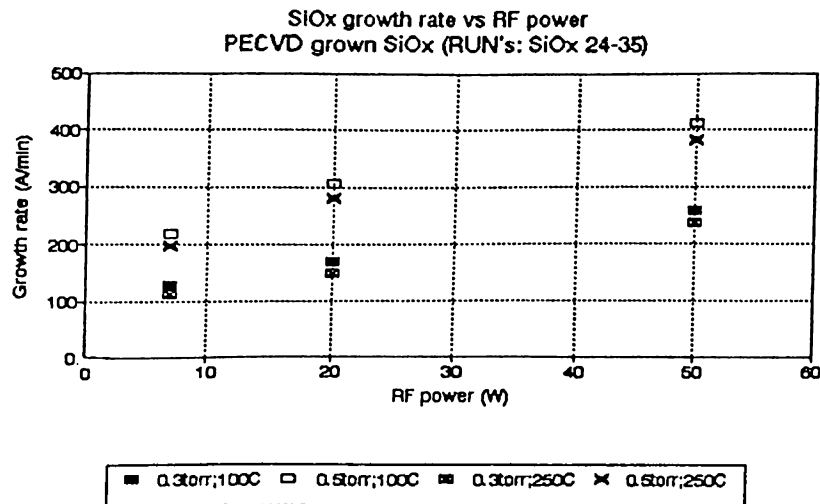


Figure 3.20: RF power (W) vs. Growth Rate (Å/min)

big areas as well as in small openings down to  $1\mu\text{m}$ . Applying such a technique in our process-flow gave us the ability of using only one lithography step. Otherwise, after stripping the resist and applying PECVD, one more lithography step to etch the metalization windows must be used.

### 3.7 Metalization

In the metalization steps Leybold LE-560 box coater was used. With this machine tungsten boats (tantalum for Ge) were used as thermal evaporator. After calibration of the piezo crystal, all of the evaporations was carried out automatically by process control unit. Evaporations were done in the region of  $10^{-6}$  mbar. Distance between the boat and the samples were set to 15 cm. Since the amount of material evaporating from the boat reaching to distance  $d$  is given by cosine of the axial angle times the main axis (axis perpendicular to the boat) evaporation, samples and the thickness detector were placed just at the top of boat. Also to prevent cross contamination of the boats, each were screened with glass barriers.

Metalization layers and their evaporation rates are given below. For Ti and Ni, it was observed that evaporation rate depends strongly on two things. One is the amount of material in the boat which acts as thermal heat sink. Another one is the current driven to the boat which is determined by the boat resistance. Also melting points of these two materials are much higher than the others and they need more energy to evaporate. Decreasing the boat resistance and cutting Ti into small pieces can be used for increasing the evaporation rate. To ensure low contact resistances, exact surface cleaning (removing residues and oxide at the contact surface) can be done by dipping the structure into buffered HF followed by DI water rinsing and drying. Any water left on the surface causes degradation of ohmic contact in time.

Material	Melting Point (°C)
Ge (Germanium)	937
Au (Gold)	1062
Ni (Nickel)	1453
Ti (Titanium)	1675

p-type Metalization Layers :

- Ti 200 (Å) at 5 (Å)/sec.
- Au 2000 (Å) at 15 (Å)/sec.

Since our p-type region is highly doped, normally any metal which is put under such vacuum conditions by evaporation, shows ohmic characteristics. Adhesion to the surface is achieved by alloying and sintering. Putting Ti before gold metalization results in much better adhesion of Au to surface and in this way decreasing the serial resistance. Au is preferred for final metalization layer. It gives us low contact resistance as well as soft surface quality for bonding purposes. Important thing is to keep Ti evaporation rate at high enough values to avoid titanium oxide formation during metalization. Low oxidations can be tolerated by cracking oxide at 480°C.

Following p-type metalization, soft annealing in Ar<sub>2</sub> atmosphere at 460°C for about 1 min was done. The aim of this annealing is to get the metal to stick to the surface for further process steps, since in the thinning part and n-type metalization, p-type surface was exposed to mechanical stresses between clampers and the metalization disk. Any stripping of the metal from the surface can cause etching of the surface and lifting the whole metalization. This soft annealing procedure also helps to the increase of native-oxide and deposited SiO<sub>2</sub> densification.

### 3.7.1 Thinning

After metalization of *p*-side, thinning was applied to the *n*-side before *n*-type metalization. Aim of this thinning is to decrease the thickness of the chip to about 100μm. Thinner chips has lower heat capacities and show less resistances to applied current pulses. Thinning values which are less than 100μm are not preferred in order to avoid cracking and to increase the life time of the crystal even though cleaving is much easier in this case. Instead of lapping and polishing, thinning was done by dynamical chemical wet etching of the *n*-side. Laser

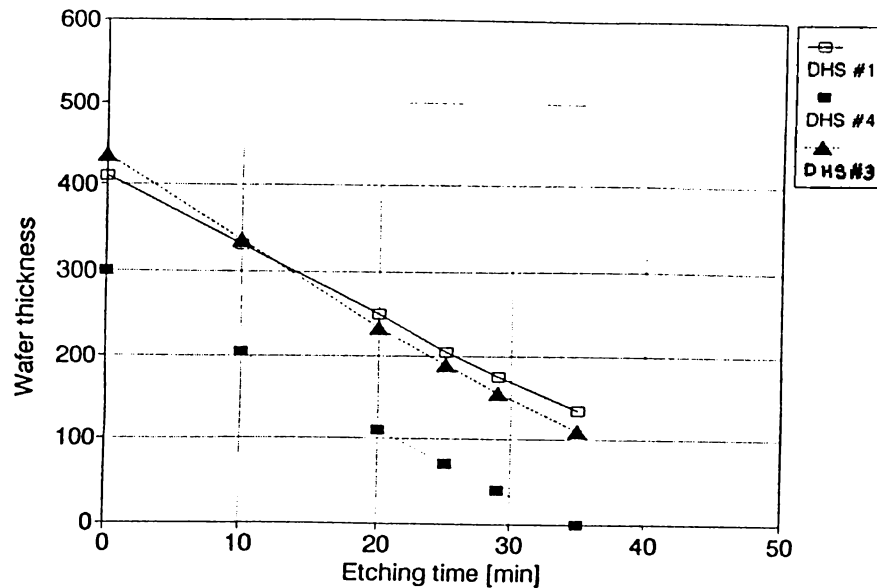


**Figure 3.21:** Thinning characteristic of GaAs wafers in Ammonia sol.+  $H_2O_2$  (1:10)

structures were first stuck to microscope slides with photoresist by putting the *p*-type side down and then baked at  $85^\circ\text{C}$  for about 30 min. Baking temperature and time was found to be crucial. Because of the exothermic nature of the dynamical thinning, any kind of bubbling in the photoresist during the baking step results in thinning failures. After baking the photoresist samples were put into thinning solution. Thinning was done in a dynamical way and solution used for this purpose was : Ammonia solution ( $NH_3$  25%) + Hydrogen peroxide ( $H_2O_2$  30%) with 1:10 volume ratio respectively. With this solution an average etching performance of  $8\mu\text{m}/\text{min}$  to  $10\mu\text{m}$  was achieved in dummy  $Al_{0.3}Ga_{0.7}As$  samples (figure 3.21). Chip thicknesses were lowered down to  $110\mu\text{m}$  in average.

After this thinning process laser structures were put into a polishing solution which was showing a smooth etching characteristics. For this aim phosphoric acid ( $H_3PO_4$ ) + hydrogen peroxide ( $H_2O_2$ ) + DI water were mixed with the volume ratio (1:1:5) respectively. Samples were further etched  $4\mu\text{m}$  in this solution to get much uniform surface for metalization.

Following the thinning process n-type metalization was performed with the following metalization layers:

- Ge 350 (Å) at 5 (Å)/sec.
- Au 600 (Å) at 15 (Å)/sec.
- Ni 250 (Å) at 5 (Å)/sec.
- Au 1500 (Å) at 15 (Å)/sec.

### 3.7.2 Annealing

Annealings were done in AG-610 minipulse RTP device. RTP device was first purged with argon ( $\text{Ar}_2$ ) for about three minutes to get rid off the water inside. Samples are then put onto the Si wafer carriage. By increasing the current in the tungsten halogen flash lamps step by step  $480^\circ\text{C}$  was reached. Samples were annealed at  $480^\circ\text{C}$  in  $\text{Ar}_2$  atmosphere for about one minute. Continuous flow of  $\text{Ar}_2$  was kept until temperature dropped to  $140^\circ\text{C}$ . After annealing, samples were investigated under Olympus reflected and transmitted light metallurgical research microscope model:BHSM 313-U. Metalization quality was checked by scratching the surface by another metal. No striping and peeling of the metalization was observed.

In metalization, one of the aim is to obtain suitable surfaces for outer connections. Lower rates of evaporation are preferred for thin layers while higher rates can be used in thicker metalization layers. After metalization, devices are connected to the outer world by wires and bonding pads. Bonding can be done in different ways but thick enough Au always serves as a soft surface.

One important parameter to determine the quality of the contact is series resistance ( $R_s$ ) which effects the performance of the device directly. High series resistances may cause heating of the chip resulting in shifting of laser working frequency. Even in worst cases, at very high pumping rates device failures can be seen. In the above annealing procedure, the temperature is the most the critical parameter since excess temperatures can destroy the ohmic contact as

well as the  $p$ - $n$  junction parameters. Depending on the annealing oven type and furnace geometry, temperatures may change from one process to another. Most flash lamp annealers have the advantage of quick temperature rise as well as good temperature control by the driving current.<sup>62</sup>

Performance of the metalization process for laser diode structures can be seen in the series resistance calculations from the observed I-V curves. Normally series resistances must be few ohms.



# Chapter 4

## Characterization

### 4.1 Laser diode parameters

Laser diodes are characterized by several parameters. Some of them and their short definitions can be given as follows:

- Forward Current  $I_f$  : It is the current which is seen through the laser diode under forward bias conditions.
- Threshold current  $I_{th}$  : It is the current where laser diode begins to generate laser light output. In other words it is the limit, that is separating spontaneous emission and stimulated emission regimes. Threshold current of a laser diode can be found from the  $I_f$  vs. absolute power output measurements.
- Reverse Voltage  $V_r$  : It is the maximum voltage that can be applied to the device in reverse bias before breakdown occurs.
- Operating current  $I_{op}$  : It is a current to obtain specific light power output.
- Wavelength  $\lambda$  of the device is defined as : For single-mode operating diodes it is the wavelength of the single spectral line of the laser output. For a multi-mode device, it is the wavelength of the maximum intensity line in the emission spectra.

- Near field pattern : It is the light intensity distribution of electromagnetic field just at the laser facet.
- Far field pattern : Light intensity distribution beginning in the region of mm's away from the laser facet. Theoretically it is the direct fourier image of the near field distribution.
- Radiation angles  $\theta_{||}$ ,  $\theta_{\perp}$  : They are defined as the full width at half maximum in the intensities of the far field pattern, both in lateral and transverse directions to the junction plane.
- Differential efficiency  $\eta_D$  : The mean value of the incremental change in the optical power output for an incremental change in forward current.

## 4.2 I-V Characterization and Series resistance $R_s$

Voltage, current dependences of the laser diodes was obtained by using a Hewlett-Packard HP4142 DC source and monitoring test system. In this measurement we first looked at whether our chips were showing the I-V characteristic of a diode. After approving that we have a good *p-n* junction, forward and reverse I-V behavior of the laser diodes were studied. Reverse current values were restricted to 1 mA, while forward current limit was taken as 100 mA. No breakdowns were observed for the reverse voltage values down to - 4 volts. Samples were not driven further in reverse bias for the fear of an excessive current during breakdown which may damage the diode. From the forward voltage current graphs which shows good I-V characteristics of a diode, series resistance values were calculated by the simple ratio of differential changes in the forward current to forward voltage values.

Typical observed I-V characteristics gave us series resistance values changing in the range 3 to 12 ohms figure 4.1. The series resistance value  $R_s$  is given as

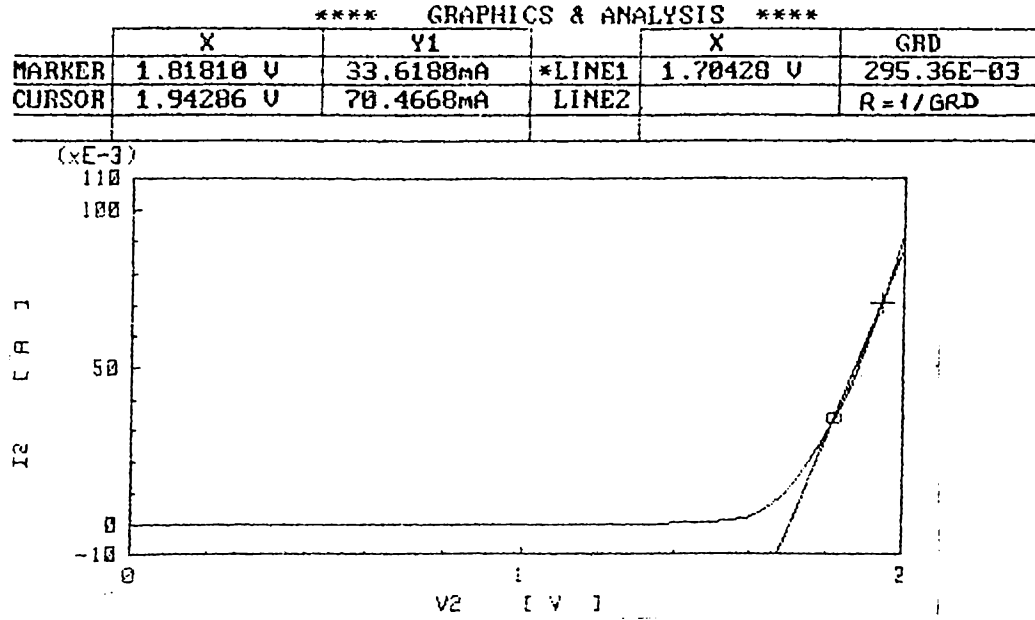


Figure 4.1: I-V Characteristic of the GRINSCH Laser Diode

$R_s = 2R_c + R_b$ . Where  $R_b$  is the resistance of the bulk material and  $R_c$  is the specific contact resistance. Resistance of a slab of a material is given by.

$$R = \rho \frac{l}{A}$$

where  $\rho$  is the resistivity,  $l$  is the length and  $A$  is the crosssectional or contact area. This formula is valid for bulk resistance value  $R_b$ . Specific contact resistance calculations can be done by different measuring techniques such as transmission line method.<sup>41</sup> As it was mentioned in the metalization part, series resistance of a laser diode appears as an important parameter. High series resistances cause heating of the laser diodes and also shift the working frequency. Series resistance values obtained in this work which are given in the table below show that good ohmic contacts with low specific resistivity for both  $p$  and  $n$  type contacts were achieved in the metalization.

Cavity length $\mu\text{m}$	Stripe Width $\mu\text{m}$	$R_s$
134	5	8.39
201	5	3.85
375	12	4.81
389	5	9.06
429	12	7.48
563	5	7.45
791	12	3.52

### 4.3 Emission spectra of the GRINSCH

Emission spectra of the lasers were studied for different  $I_f$  values. In order not to heat up the laser diode while it is working, short current pulses of pulse-width 550 nsec with the repetition frequency 10 kHz was used throughout the characterization. A 1 meter Jobin Yvon double-grating monochromator was used along with a GaAs photomultiplier, and the standard photon counting techniques were applied to collect the spectra. Overall resolution of the system was 1.9 Å. The sample was placed 6 cm away from the slits without any optics.

#### 4.3.1 Optical resonant cavity and its modes

To produce lasing action in our laser diode structure, generated light in the medium must be confined into a Fabry Perot like cavity. To achieve this, diodes are first cleaved into bars with various cavity lengths along their main axes to form mirrors. Cleaved mirror faces of GaAs shows reflectance of  $R=0.32$ . From these bars chips of the laser diodes were obtained by cutting. By this way our laser chips act as a Fabry Perot cavity and select their own laser oscillation modes. These operating modes are the longitudinal and transverse optical modes of the cavity.

An oscillation mode in a resonant cavity can be thought as the standing waves

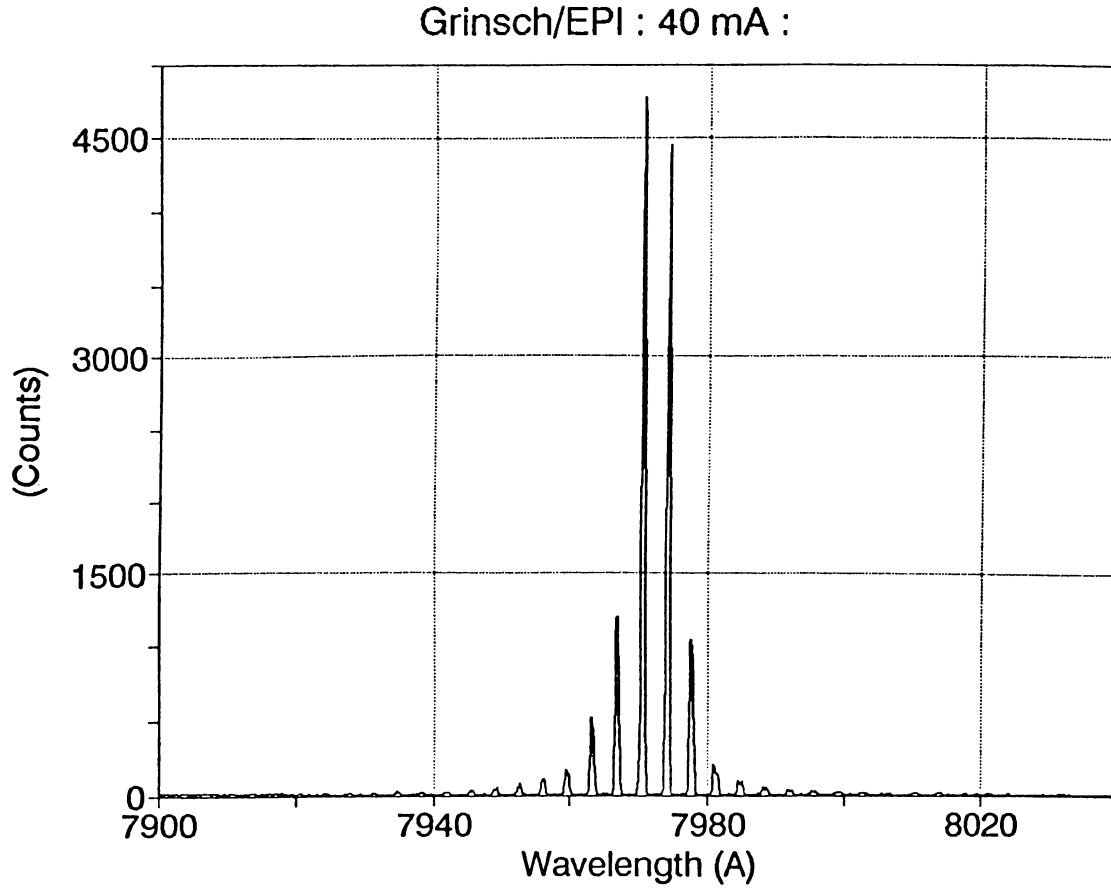


Figure 4.2: Lasing emission spectra of the GRINSCH laser diode

on a stretched string pinned at both ends. Only the modes corresponding to multiples of half a wavelength can be supported by the constructive interference and all other modes will die away. Equation for longitudinal modes is given by,

$$L = \frac{\lambda}{2n} \times q$$

where  $\lambda$  is the wavelength,  $L$  is the cavity length,  $n$  is the refractive index of the medium (3.5 for GaAs) and  $q$  gives the number of modes which can be supported by the cavity.

For a GRINSCH laser diode of  $250\mu\text{m}$  cavity length, wavelength was observed to be around  $7972 \text{ \AA}$  in multimode operation. For this cavity length,  $q$  takes on

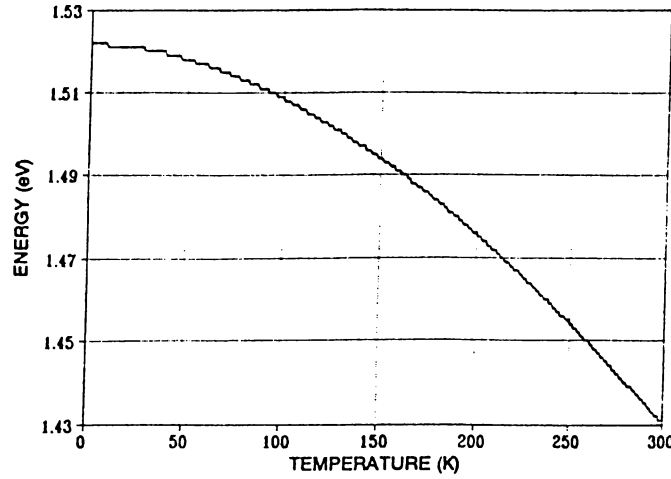


Figure 4.3: Dependence of the band-gap energy of GaAs on temperature.

values more than 2000 (exact value is 2195). Change in the  $q$  value by one causes a wavelength variation of  $\Delta\lambda$  around  $3.63 \text{ \AA}$ , which matches the value observed between the modes in the lasing emission spectra at 300K (figure 4.2).

### 4.3.2 Effect of operating temperature on the emission wavelength

In a laser diode, laser oscillation arises at the wavelength with the maximum gain, which is determined by the band-gap energy  $E_g(t)$ . This band-gap energy has temperature dependent characteristics. Increasing or decreasing the temperature causes broadening or squeezing in the energy levels of the lattice atoms. This causes a decrease in band-gap energy when temperature is raised or an increase when it is lowered. Temperature dependence of the energy-gap of many semiconductors has been fitted by the following empirical relation,<sup>63</sup>

$$E_g(t) = E_g(0) - \frac{\alpha \cdot T^2}{T + \beta}$$

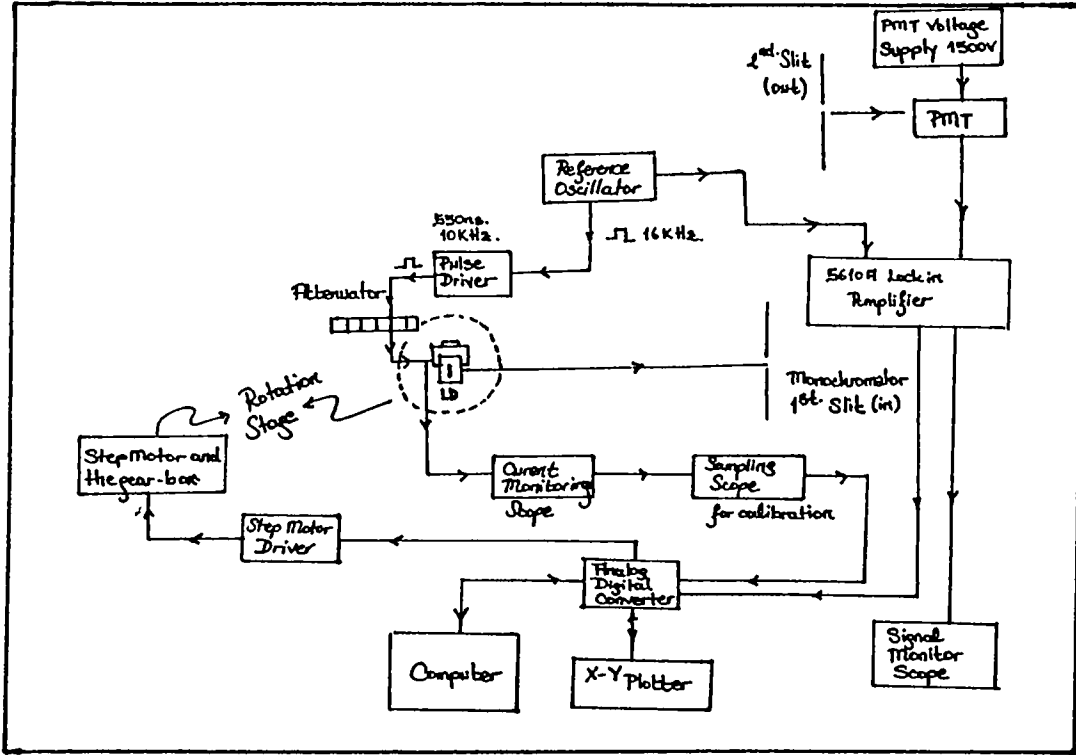


Figure 4.4: I-P Measurement setup

where  $E_g(0)$  is the value of the energy band-gap at 0 Kelvin and  $\alpha$  and  $\beta$  are material constants. For GaAs at the direct band-gap edge:  $E_g(0)=1.5216$  eV,  $\alpha=8.871 \times 10^{-4}$ ,  $\beta=572$ . With these given values intrinsic GaAs shows the dependence on temperature as given in figure 4.3.

## 4.4 I-P Characterization

Cleaved laser chip cavity lengths were measured under an optical microscope within  $\pm 3\mu\text{m}$  and I-P measurements were done for different cavity lengths varying between 100 to 900  $\mu\text{m}$ . From the obtained I-P graphs, by linear approximations, corresponding  $I_{th}$  and differential quantum efficiency values were obtained.

Setup in Figure 4.4 was used in the I-P characterization of the laser diodes. In this setup by the help of a computer program, applied current and total absolute power output of the laser diode (for one mirror) was obtained simultaneously.

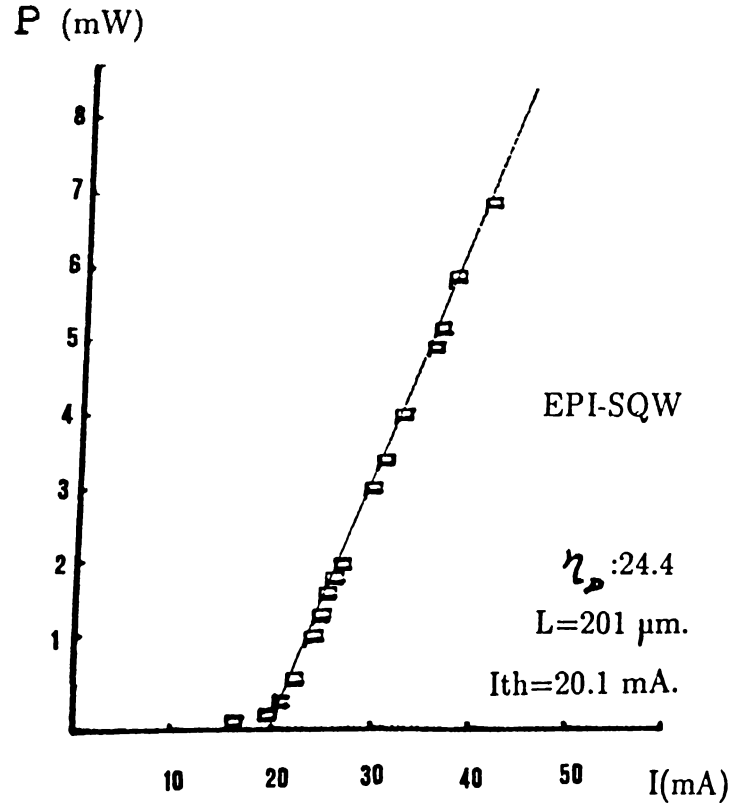


Figure 4.5: I-P characteristic of GRINSCH

A detector which was calibrated over a wide range of wavelengths was used for measuring the absolute light output. A lock-in amplifier was used to extract the signal from the environmental noise. In calibration and reference readings a high frequency sampling scope was used.

#### 4.4.1 Threshold Current

A characteristic I-P dependence of the GRINSCH laser diodes is given in figure 4.5. Dependence of the output power on driving current was seen as linear above the threshold (i.e. there is no kinks in the I-P graphs). These kink free graphs show that our lasers are working in the fundamental mode of  $TEM_{00}$ .



operation.

Threshold current values are found for different cavity lengths for two different cavity widths of  $5\mu\text{m}$  and  $12\mu\text{m}$ . Threshold current densities are drawn with respect to the cavity length  $L$  as shown in figure 4.6.  $12\mu\text{m}$  width lasers showed lower threshold current densities compared to  $5\mu\text{m}$  ones. For  $263\mu\text{m}$  cavity length, threshold current density was found as  $1.2\text{ (kA/cm}^2\text{)}$  in  $12\mu\text{m}$  stripe lasers, whereas  $2\text{ (kA/cm}^2\text{)}$  was obtained for  $5\mu\text{m}$  cavity width lasers. Although rapid increase in the threshold current density is expected below  $10\mu\text{m}$  cavity width which is shown to be true by previous studies,<sup>64</sup> high threshold current densities for  $12$  and  $5\mu\text{m}$  cavity widths imply that uniformity inhomogenities occur along the ridge structures after the RIE processing. These high  $J_{th}$  values also show that effective width of the stripes are less than the value obtained after photolithography. We can say that  $5\mu\text{m}$  stripes are much more effected from the  $\text{CCl}_2\text{F}_2$  dry etching process.

It was observed that threshold current density  $J_{th}$  depends on the cavity length  $L$ . The threshold current density takes its minimum value for the long cavity samples, but the minimum threshold currents were obtained at shorter cavity lengths. Since  $I_{th}$  is given by the following relationship:

$$I_{th} = W_a L J_{th}$$

where  $W_a$  is the width of the stripe and  $L$  is the cavity length.  $I_{th}$  decreases with decreasing the cavity length (figure 4.7). It was shown that leakage current increases as the cavity becomes larger.<sup>71</sup> Which means increase in leakage current is seen for long cavity lasers as well as for the larger cavity widths causing an increase in  $I_{th}$  values. Decreasing the cavity length further causes an increase in the  $I_{th}$ . This feature is expected from the theory. Since gain at the threshold is given by:

$$\Gamma g_{th} = \alpha_i + \frac{1}{L} \ln \frac{1}{R}$$

where  $\Gamma$  is the optical confinement factor,  $\alpha_i$  is the internal loss,  $L$  is the cavity length. Internal loss  $\alpha_i$  calculation for different cavity length lasers is given in

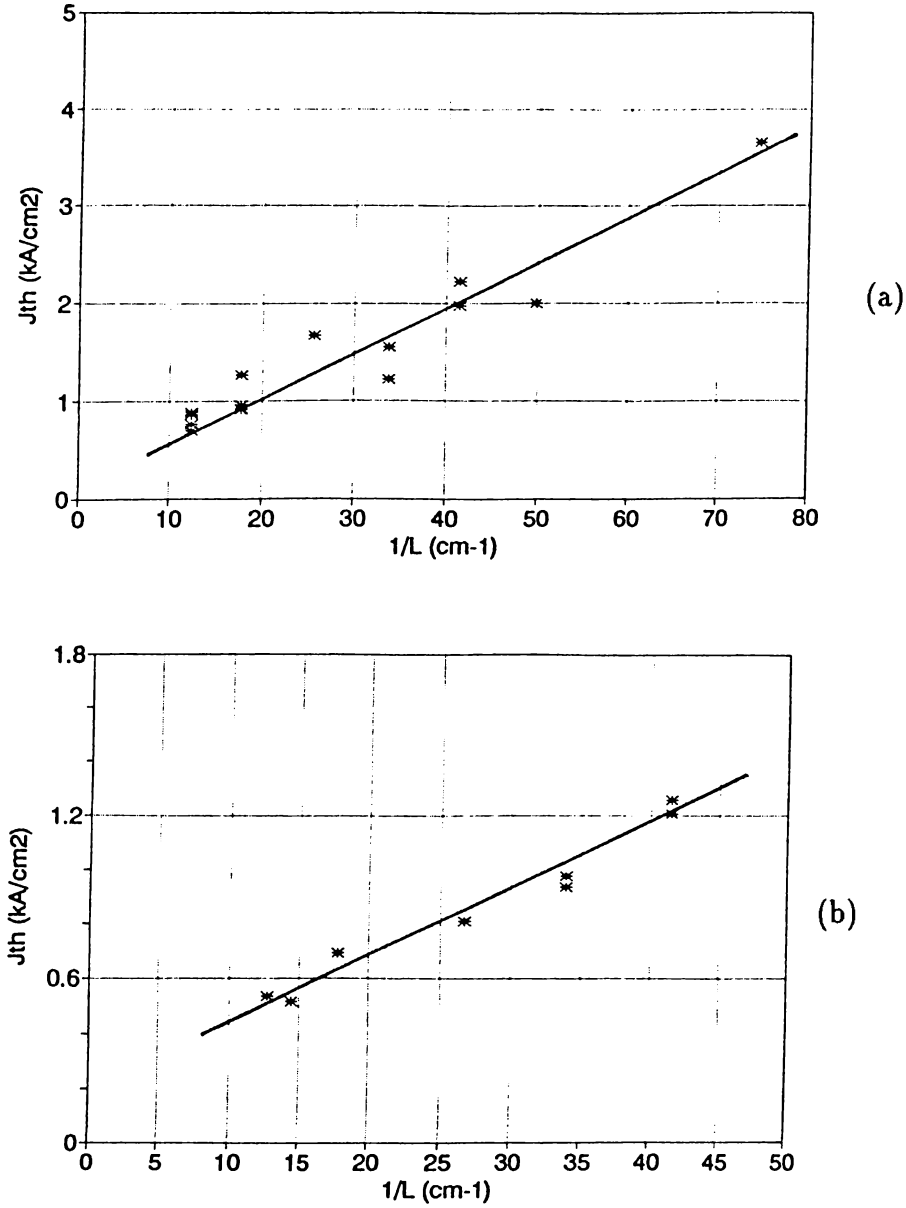


Figure 4.6:  $J_{th}$  vs.  $L$  (a) For  $5\mu\text{m}$  stripe width (b) For  $12\mu\text{m}$  stripe width

the quantum efficiency section. As  $L$  becomes smaller, the mirror loss term  $L^{-1}\ln(R^{-1})$  increases rapidly and a larger gain is needed to sustain the lasing. Minimum  $I_{th}$  obtained in the laser chips was 18 mA for a  $295\mu\text{m}$  cavity length. These obtained data for both  $J_{th}$  and  $I_{th}$  show familiar features with the previous work done by Kurobe *et al.*<sup>71</sup> where minimum  $I_{th}$  was obtained as 10 mA at an

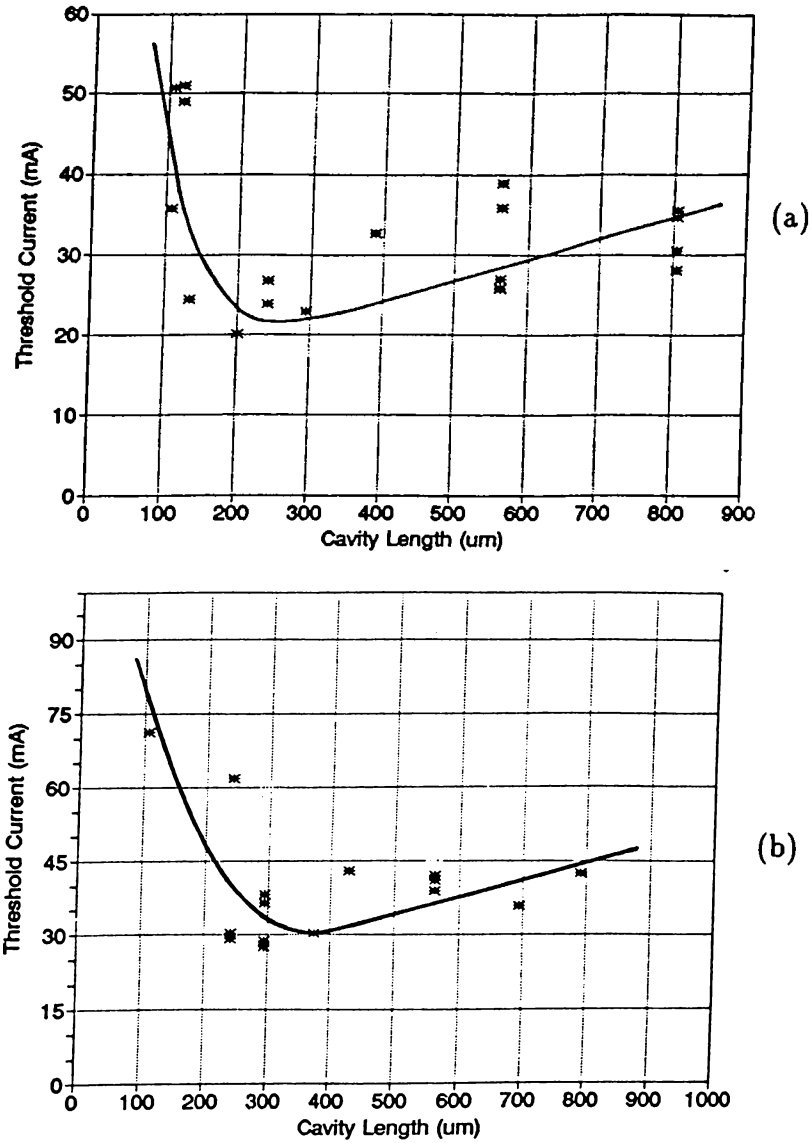


Figure 4.7:  $I_{th}$  vs.  $L$  (a) For  $5\mu\text{m}$  stripe width (b) For  $12\mu\text{m}$  stripe width

optimal cavity length of  $200\mu\text{m}$ .

The Confinement factor or filling factor  $\Gamma$  was previously studied on double heterostructures by Hakki and Paoli<sup>68</sup> and is defined as:

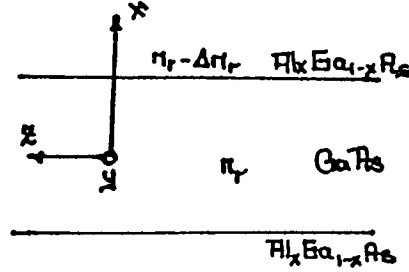


Figure 4.8: Schematic of the waveguide and reference coordinates.

$$\Gamma = \frac{\int_{-d/2}^{d/2} E_y^2(x) dx}{\int_{-\infty}^{\infty} E_y^2(x) dx}$$

In this relation  $E_y$  represents the TE mode component along the y axis as shown in figure 4.8

The electric field for even modes has the functional form,

$$\begin{aligned} E_y &= E_0 \cos(k_x x) \exp(-jk_z z), & |x| < \frac{1}{2}d \\ &= E'_0 \exp(-k'_x |x|) \exp(-jk_z z), & |x| > \frac{1}{2}d \end{aligned}$$

where the propagation constants  $k_x$  and  $k_z$  are obtained from the solutions of the characteristic equation

$$\Psi \tan \Psi = \Psi'$$

noindent where  $\Psi = \frac{1}{2}k_x d$ ,  $\Psi' = (A^2 - \Psi^2)^{1/2}$  and  $A = (\pi n_r d / \lambda)^2 [2\delta n_r / n_r - (\delta n_r / n_r)^2]$ . In the definition of  $A$ ,  $n_r$  and  $n_r - \delta n_r$  are the refractive indices in the regions  $|x| < \frac{1}{2}d$  and  $|x| > \frac{1}{2}d$  respectively,  $d$  is the thickness of the waveguide, and  $\lambda$  is the wavelength in free space. Solution of the filling factor  $\Gamma$  for the TE mode is given by:

$$\Gamma_{TE} = \left( 1 + \frac{\sin(2\Psi)}{2\Psi} \right) \left[ 1 + \frac{1}{\Psi'} \left( \frac{A \cos(\Psi^2)}{\Psi} \right)^2 \right]^{-1}$$

Similar analysis can be carried out for the TM mode in double heterostructures. For a GRINSCH structure analysis comes with the addition of the graded index layer where electrical field is defined by the standard Airy functions. In a study by Chinn<sup>73</sup> analysis of the confinement factor  $\Gamma$  in GRINSCH single Quantum Wells was carried out and dependence on graded index layer thickness and quantum well width was shown. For our GRINSCH single quantum well confinement factor seems to be 3-5 %.

#### 4.4.2 Differential quantum efficiency $\eta_D$

One facet differential quantum efficiencies were obtained for each laser chip from the I-P graphs using a computer program. Obtained results are given in figure 4.9. Calculated differential efficiency is given by,

$$\eta_D = \frac{e \Delta P}{\Delta I E_g}$$

where  $e$  is the electron charge,  $\Delta P$  is the differential change in power in Watts (for one facet of the laser cavity),  $\Delta I$  is the differential change in current in Amperes, and  $E_g$  is the bandgap energy. We can give the same formula with the internal quantum efficiency  $\eta_i$  as follows:

$$\eta_D = \eta_i \frac{\frac{1}{L} \ln \frac{1}{R}}{\alpha_i + \frac{1}{L} \ln \frac{1}{R}}$$

If we take  $\eta_i \cong 1$ , we can extract the internal absorption as,

$$\alpha_i = \frac{1}{L} \ln \frac{1}{R} \left( \frac{1}{\eta_D} - 1 \right)$$

Calculated internal losses for different cavity lengths are given in the table below. Since internal loss does not depend on the stripe width, stripe widths are not shown in the table. In a study given by Micheal *et al.*<sup>72</sup> internal losses of about  $2\text{cm}^{-1}$  were achieved which gave the ability of observing the second quantized state lasing in the lasing emission spectra of the single quantum wells. Since our internal loss values  $\alpha_i$  are not small enough to observe such a feature

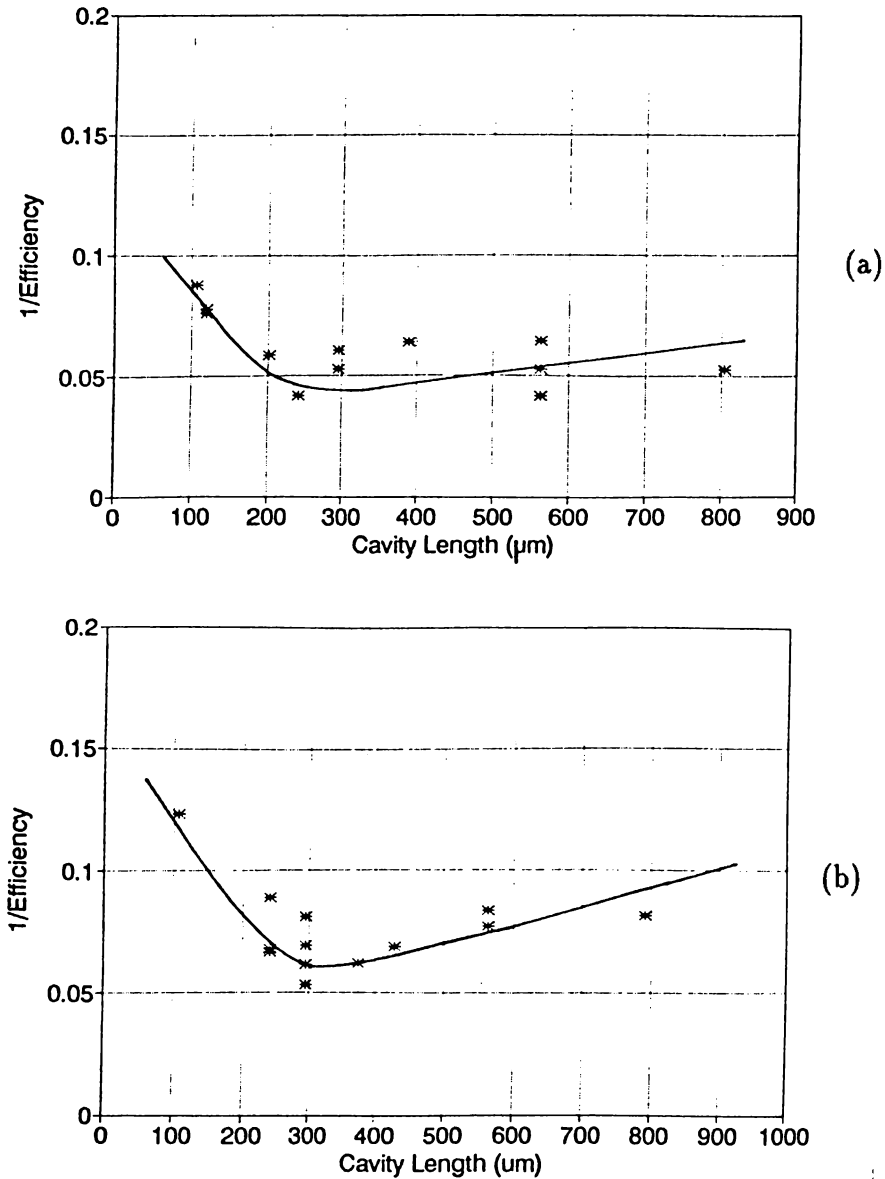


**Figure 4.9:**  $1/\text{Differential Quantum Efficiency } 1/\eta_D$  vs. cavity length  $L$ , (a) For  $5\mu\text{m}$  stripe width (b) For  $12\mu\text{m}$  stripe width.

second quantized level transitions were searched from the spontaneous emission spectra. High internal loss coefficients observed during these experiments may be explained by mirror quality. Since the separation of the chips was done manually mirror quality was not as good for short cavity lasers as in long cavity lasers. This

can be a reason for obtaining almost the same differential quantum efficiency for different cavity lengths in the shorter cavity length domain.

L ( $\mu\text{m}$ )	( $\eta_D$ )	$\alpha_i$ ( $\text{cm}^{-1}$ )	L ( $\mu\text{m}$ )	( $\eta_D$ )	$\alpha_i$ ( $\text{cm}^{-1}$ )
107	16.6	100	295	16.5	36.29
107	11.4	94.15	295	19	36.59
120	12.8	87.53	389	15.6	27.41
120	13.1	87.70	563	19	19.17
134	21.8	81.13	563	23.3	19.4
201	24	54.3	695	19.7	15.56
241	15.1	44.15	804	19	13.4
241	11.3	43.1	804	21.6	13.52

For long cavity lengths high differential quantum efficiencies up to 26.7 % for 563 $\mu\text{m}$  and 23.5 % for 804 $\mu\text{m}$  cavity lengths were obtained. Eventhough these high  $J_{th}$  values show that some inhomogenities present in the ridge structure, process was good enough to yield long cavity high power lasers. In this wavelength region total differential efficiency of 53.4 % for 563 $\mu\text{m}$  cavity lasers matches the previously obtained results by several workers.<sup>29</sup>

Figure 4.9 also shows that an optimal length for 5 $\mu\text{m}$  stripe width lasers is  $L_{op}=241\mu\text{m}$  (with  $\eta_D=24$  % and  $I_{th}=23.9$  mA) and for 12 $\mu\text{m}$  width stripes, optimal length is  $L_{op}=295\mu\text{m}$  (with  $\eta_D=18.8$  % and  $I_{th}=27.6$  mA), where we see the maximum efficiencies with minimum threshold currents.

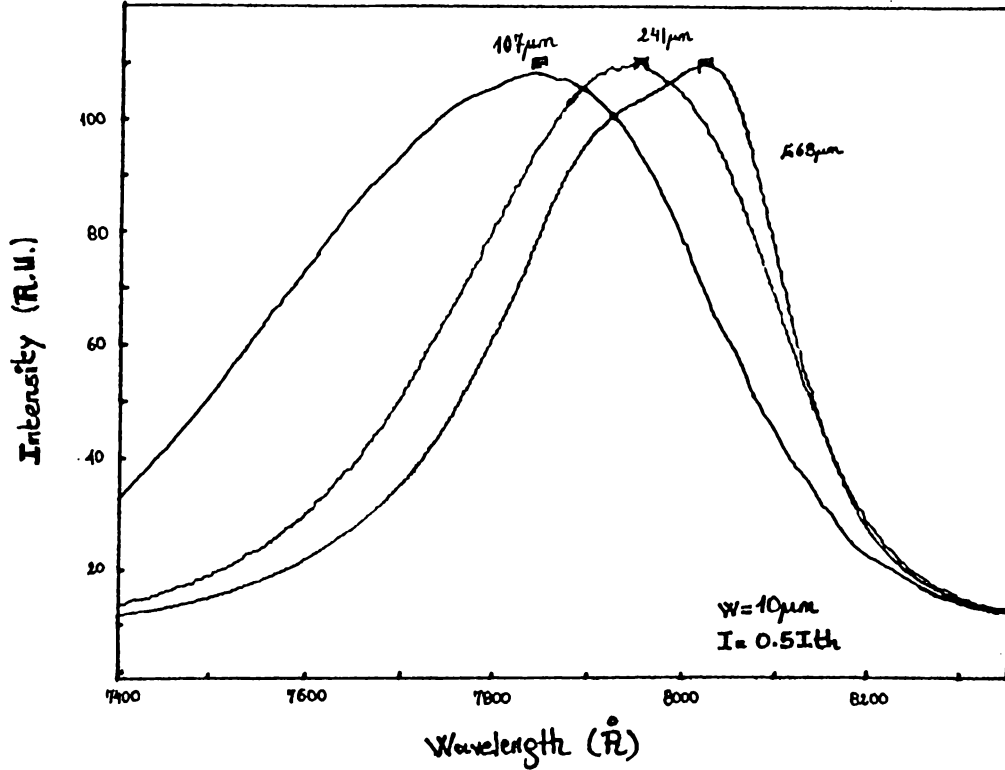


**Figure 4.10:** Spontaneous emission spectra at different cavity lengths. Peak positions of the spectra are shown by rectangles.

## 4.5 Spontaneous Emission and Lasing

Spontaneous emission spectra of the GRINSCH structure was taken at different cavity lengths for different driving currents. In the low current region the shape of the intensity profile does not depend on the current.

In figure 4.10 at half the threshold current values for different cavity lengths shift in the spontaneous emission peak position is given. This shift in the wavelength is due to the change in the threshold gain  $g_{th}$  when cavity length is changed. Increase is seen for  $g_{th}$  at short cavity lengths causing the shift in the peak position to lower wavelengths. These spontaneous emission spectra also show very small range of adjustability of the wavelength of the output light by changing the cavity length. One can see that spontaneous full width at half



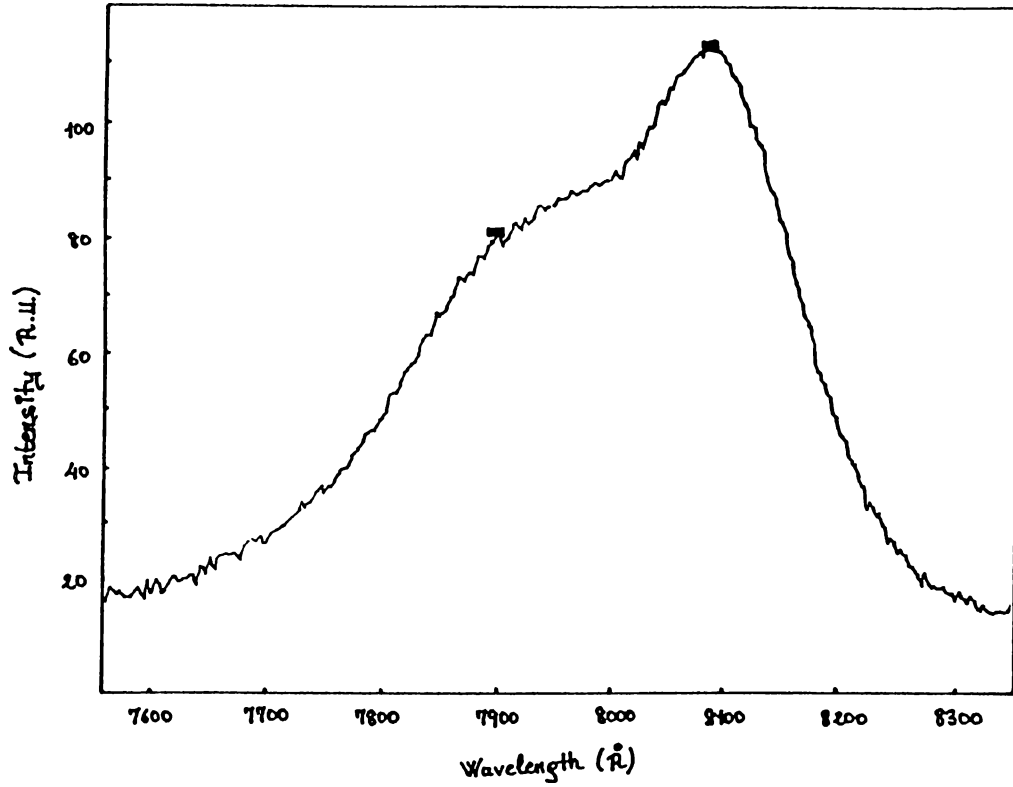


**Figure 4.11:** Spontaneous emission spectra at  $804\mu\text{m}$  cavity length is showing two transitions between the edges of the  $1e-1lh$  subbands and  $1e-1hh$  subbands.

maximum value also decreases upon increasing the cavity length.

Another interesting feature of figure 4.10 is the onset of the observation of  $1e-1lh$  and  $1e-1hh$  transitions for long cavity lengths. This is the same effect of cavity length on  $g_{lh}$  allowing the appearance of these transitions because of its low value for long cavity lengths. In figure 4.11 for the cavity length of  $804\mu\text{m}$   $1e-1hh$  transition is seen around  $8080\text{ Å}$  whereas calculated value is  $7970\text{ Å}$  and  $1e-1lh$  transition is seen around  $7890\text{ Å}$  which has a calculated value of  $7720\text{ Å}$ . Separation between the energy levels from the calculations is  $50\text{ meV}$  and from the observed transitions is  $37\text{ meV}$ . In several other works also emission spectra have been observed at longer wavelengths than predicted in the models.<sup>65,66</sup>

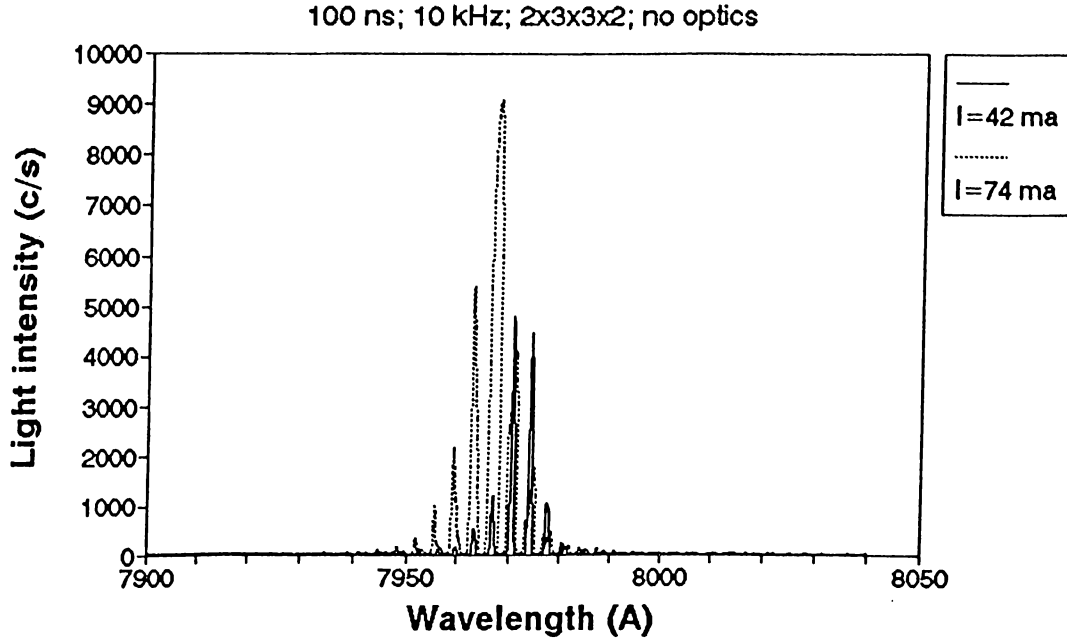


**Figure 4.12:** Lasing emission spectra of GRINSCH at two different current values.

Main contributions to this effect are spectral broadening from intraband relaxation, bandgap renormalization from many-body interactions and temperature dependent bandgap characteristics. In modeling of GRINSCH SQW lasers a study by Chinn *et al.*<sup>67</sup> shows nearly the same amount of difference between the model and the experimental data. In that study, theory gives 22 meV separation for a 75 Å SQW GRINSCH whereas measured spectra shows a 16 meV separation between the transition energies.

Spontaneous emission peak position is observed to be shifting to the shorter wavelengths as the driving current is increased. This is the direct result of the shift in the quasi Fermi levels by the increase in excess carrier density. For 107  $\mu\text{m}$  cavity length this shift is given in the table below. Same feature is also seen in the lasing emission spectra which is given in figure 4.12.

107 $\mu\text{m}$ Cavity length		
Current $I_f$	Wavelength $\lambda$ $\text{\AA}$	$E = h\nu$ eV
0.3 $I_{th}$	7855	1.5786
0.5 $I_{th}$	7835	1.5826
0.8 $I_{th}$	7816	1.5864

From the spontaneous emission spectra one can also calculate the modal gain. Modal gain is the ratio of spontaneous emission going to one mode to the total spontaneous emission and is defined by material gain  $g$  times the optical confinement factor  $\Gamma$ . It can be calculated from the spontaneous emission regime where Fabry Perot modes begin to appear up to the lasing is seen. In this limited current regime modal gain is given by the following relation.<sup>68</sup>

$$G_m = \Gamma g = \frac{1}{L} \ln \left( \frac{\sqrt{r} + 1}{\sqrt{r} - 1} \right) + \frac{1}{L} \ln R$$

where  $r$  is the average value of the two consecutive peaks in the spontaneous emission defined as  $r_i = (P_i + P_{i+1})/2V_i$ .  $P_i$  and  $P_{i+1}$  shows the peak intensities and  $V_i$  shows the valley intensity between these peaks. Modal gain was calculated in the range of 8000  $\text{\AA}$  to 8100  $\text{\AA}$ , where we see the 1e-1hh transition as the peak position of spontaneous emission in long cavity samples. For a current value of 0.4  $I_{th}$  mean value of the modal gain was seen as 145  $\text{cm}^{-1}$ . As the current is increased to 0.6  $I_{th}$ , modal gain dropped to 126  $\text{cm}^{-1}$ . Further increase in the current to 0.8  $I_{th}$  yields a gain of 110  $\text{cm}^{-1}$ . We see that the modal gain drops as the current is increased. Increasing the current further above  $I_{th}$  gives us very high ratio of  $r$  (at 2  $I_{th}$   $r \cong 1000$ ) which takes the first term to zero in the modal gain expression and the modal gain saturates. We observed highly nonlinear modal gain behavior as a function of photon energy (eV). Saturation of the modal gain by increasing the carrier density and highly nonlinear behavior was previously observed also by Kesler *et al.*<sup>69</sup> In the same study it was shown that bandgap shrinkage shows  $n^{1/2}$  dependence on the level carrier density ( $n$ ) at low current regimes, whereas this dependence is  $n^{1/3}$  at high current regime. This

bandgap shrinkage gives a broadening in level life times resulting in a softening of the sharp density of states in the quantum well structures.

## 4.6 Far Field Pattern

Far field patterns of the laser diodes were taken by the same I-P set up. Alignment of the laser chip facets in parallel to the monochromator slit was obtained by using a He-Ne laser and a beam splitter (figure 4.13). After aligning the laser mirror, monochromator was manually tuned to a wavelength where maximum emission was observed. With the help of a computer program a rotating stage was turned in the range from  $-10$  degrees to  $+10$  degrees with  $0.1$  degree steps. Measurements were done by averaging over 1000 readings at each point of rotation. In this setup intensity of the emitted light was followed by the monochromator and a photomultiplier which sends the read measured intensity value to the computer through a lock-in amplifier with the frequency of the driving current pulse. Program took these values and plotted out as a function of rotation angle.

Far field patterns for the lateral light intensity distribution for different current values for  $5$  and  $12\mu\text{m}$  stripe widths are given in figure 4.14. As can be seen from these patterns the intensity increases fast above the threshold. For high current values same amount of increase in the driving current did not yield the same amount of intensity increase like that in the low current region. As the current reaches to the high carrier injection levels saturation of the gain begins for the laser structure. Another factor, band filling, affects the increase in the emission rate. As a result, output light intensity increases much slower until the gain reaches to another threshold gain value where second level emission for  $1-e 1-h$  transition occurs. Since our lasers were not bonded to the heat sinks we did not drive our lasers with excessive current values and gain in these measurements never reached the value of second transition level.

For  $5\mu\text{m}$  stripe width and  $563\mu\text{m}$  cavity length full width at half maximum value (FWHM) of the intensity was seen at  $\theta_{||}=5.5^\circ$ . For  $429\mu\text{m}$  cavity length but

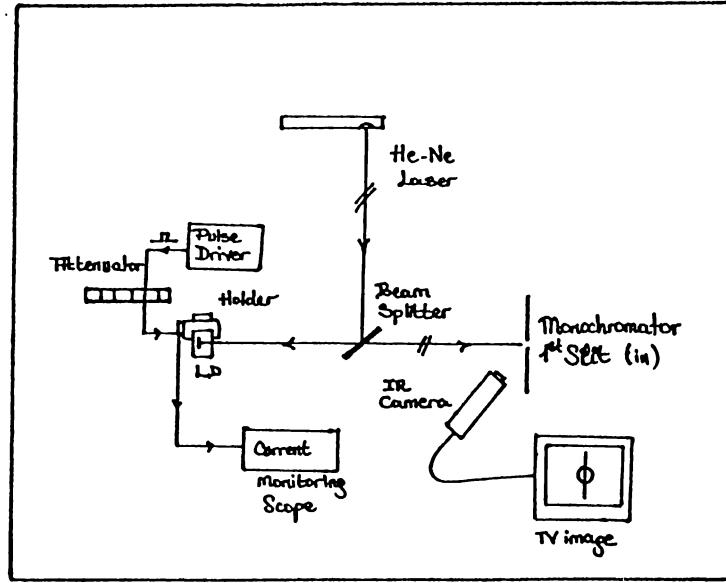
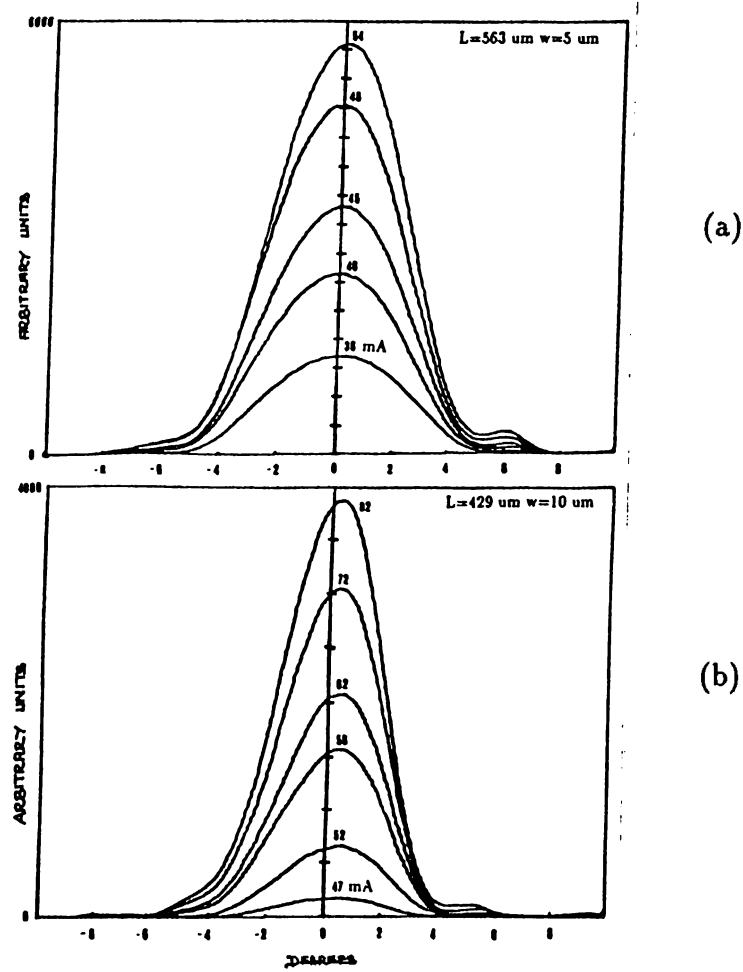


Figure 4.13: Alignment setup for far field measurement

for  $12\ \mu\text{m}$  stripe width this value was observed as  $\theta_{||}=4^\circ$ . Good confinement of the light for lateral modes was observed in each stripe width since FWHM values remained the same and no line shape change was seen even for high driving currents. Both of the far field patterns shows that GRINSCH lasers are working in the  $\text{TEM}_{00}$  fundamental mode of operation. This claim is further supported by measuring the transverse light intensity distribution for the  $563\ \mu\text{m}$  cavity length  $5\ \mu\text{m}$  stripe width which is a zero order mode distribution showing FWHM as  $\theta_{\perp}=45^\circ$  (figure 4.15).

Since our laser has a parabolically graded-index profile forming a self focusing waveguide it is much more effective in guiding electromagnetic waves. This parabolic profile is expected to sustain Hermite-Gauss modes in the direction perpendicular to the junction plane and these modes match those in the Selfoc waveguides such as Selfoc optical fibers.<sup>70</sup> Moreover, since the far field distribution is shaped by the near-field distribution, by modeling the refractive index in the laser waveguide we can not only control the propagation



**Figure 4.14:** Lateral Far Field patterns for GRINSCH laser diodes. (a)  $L=563 \mu\text{m}$   $w=5 \mu\text{m}$  (b)  $L=429 \mu\text{m}$   $w=12 \mu\text{m}$ .

characteristics and reduce the divergence of the beam, but also achieve an effective suppression of the higher order modes. But this improvement in the far field pattern gives an increase in  $I_{th}$  values since only a few mode appear in the lasing action.

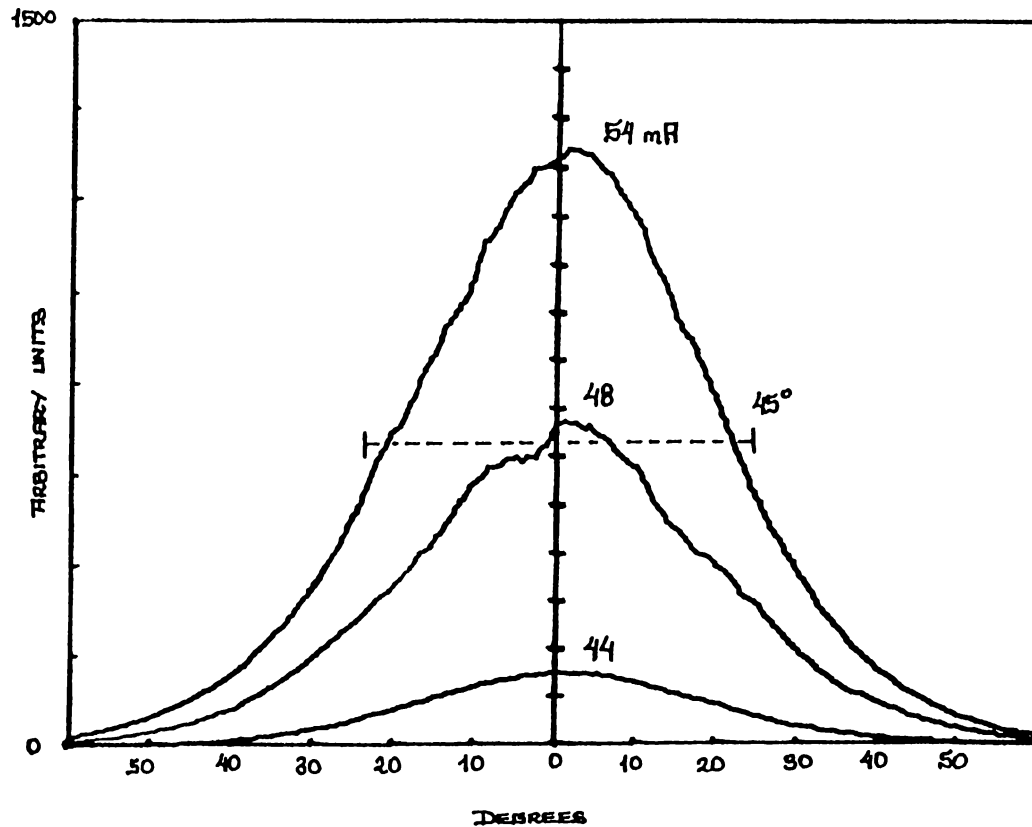


**Figure 4.15:** Transverse Far Field pattern for  $563\mu\text{m}$  long  $5\mu\text{m}$  stripe width laser diode.

## 4.7 Near Field Pattern

In near field measurements different configuration and a computer program was used (figure 4.16). First by using a He-Ne laser same alignment as in the far field measurement was done. Near field signal was focused by a lens into the monochromator slit. Then signal was divided by a beam splitter and a small fraction of it was focused over a vidicon active region to prevent destroying the vidicon. Vidicon was connected to a TV monitor for checking the focus of the beam. Incoming near field intensity was read from the TV line signal by means of a TV line-signal analyzer and a sampling scope which gives the digital output to a computer.

Near field pattern was obtained for different current values as shown in

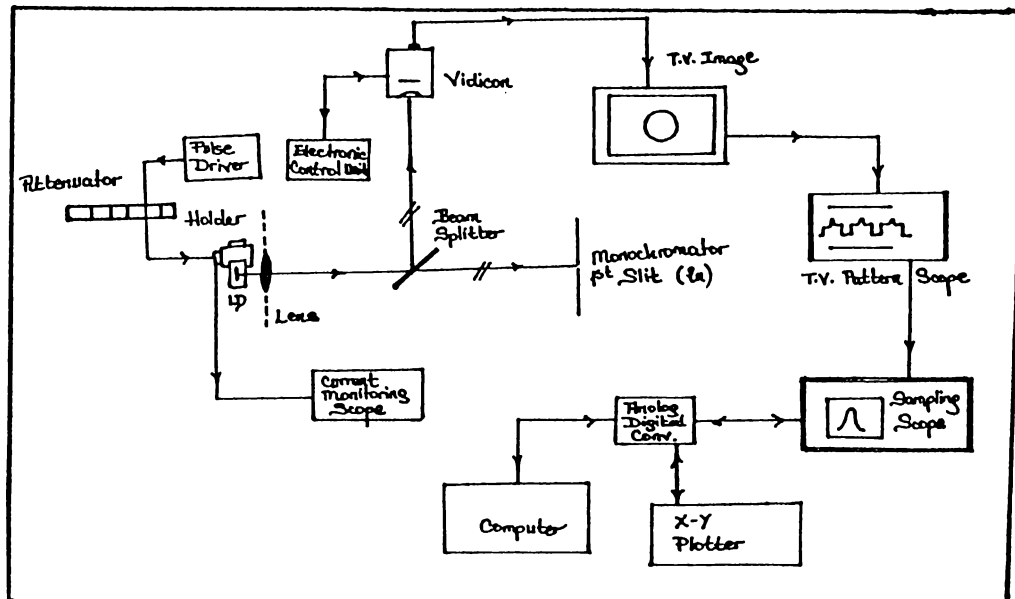


Figure 4.16: Near field measurement setup

figure 4.17. FWHM in the intensity distribution was measured from the TV signal analyzer as  $5\mu\text{m}$  which is the exact value of stripe width for this given sample. Observed hot spot region for the middle curve can be due to the dirt particles on the mirrors since the environment was not clean or due to the impurities or defects and damages coming from the growth or processing acting as recombination centers. Small intensity changes in the pattern are resulting from the vibrations in the setup since these patterns were not taken on vibration free tables.



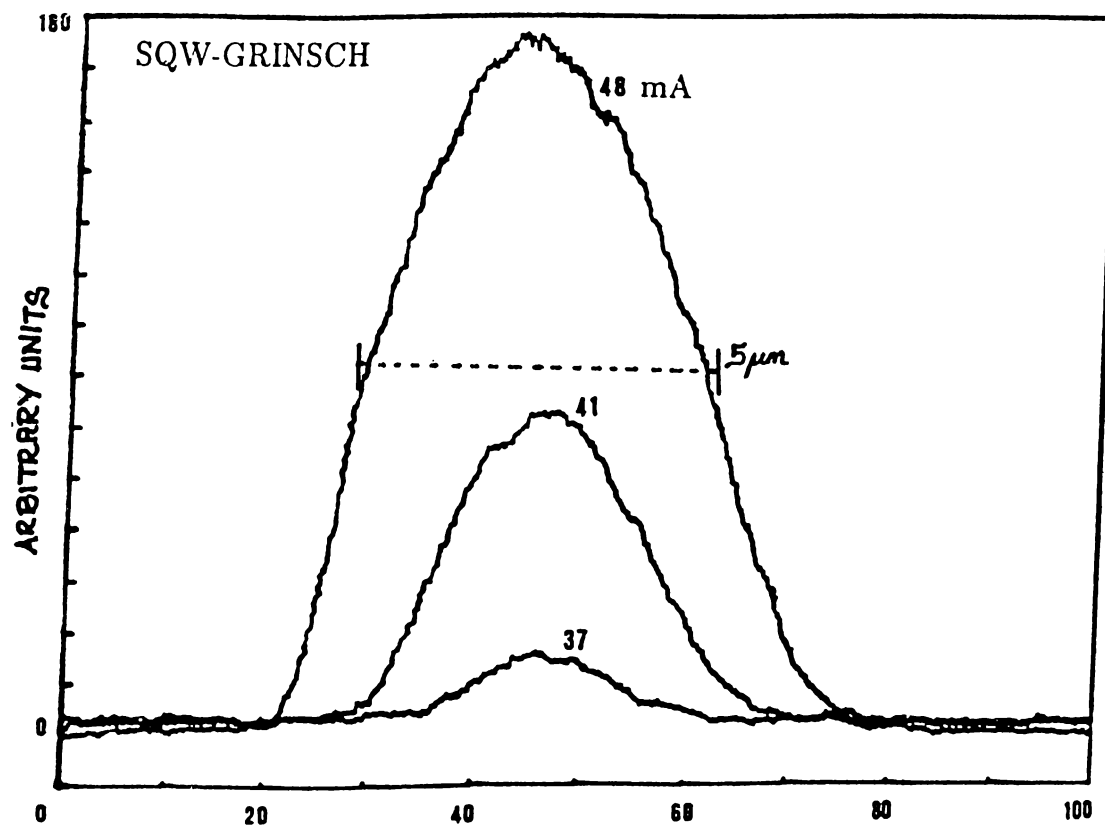


Figure 4.17: Near Field pattern of the GRISCH laser diode,  $L=563\mu\text{m}$   $w=5\mu\text{m}$

## Chapter 5

### Discussion and Conclusions

In this study design, fabrication, and characterization aspects of ridge-waveguide graded index separate confinement heterostructure single quantum well lasers of 39 Å well width was demonstrated. In fabrication of the laser diodes, MBE growth samples were etched in dry  $\text{CCl}_2\text{F}_2$  plasma in a RIE machine after patterning 5 and 12  $\mu\text{m}$  stripes by using AZ-5214E photoresist with conventional photolithography techniques. During RIE process top n-GaAs layer and some part of  $\text{Al}_x\text{Ga}_{1-x}\text{As}$  confinement layer were etched in order to obtain ridge-waveguide structure. RIE process was carried out at low pressures and relatively high self-bias voltage in order to reduce etching selectivity of  $\text{Al}_x\text{Ga}_{1-x}\text{As}/\text{GaAs}$  layers. Influence of RIE process parameters on the etching selectivity of  $\text{Al}_x\text{Ga}_{1-x}\text{As}/\text{GaAs}$  layers in Freon-12 plasma is described. After the RIE, photoresist mask defining the mesas was not removed and 100 nm thick anodic oxide layer was grown on etched  $\text{Al}_x\text{Ga}_{1-x}\text{As}$  area in order to remove RIE induced defects and have some intermediate insulation. Then, low temperature (100°C) chemical vapor deposition (PECVD) process was carried out to grow thin ( $\sim 100$  nm) layer of  $\text{SiO}_2$  on the whole structure, including ridges covered by the photoresist mask. Structural data of these low temperature  $\text{SiO}_x$  films was obtained by using FTIR and ellipsometry techniques. Data on both of these studies with various process parameters are given. Low substrate temperature deposition in PECVD gave us the ability of lifting off the photoresist mask

together with the top SiO<sub>2</sub> layer. In this way self-aligning of the ridge-stripe structures with respect to the openings in SiO<sub>2</sub> was obtained. Finally after thinning the wafers, ohmic contacts were applied onto *p*-side (Ti/Au) and *n*-side (Ge/Au/Ni/Au) of the structure. After rapid thermal annealing separation was done by cleaving the structures into various cavity lengths.

Ohmic contacts were checked from I-V characteristics of the laser diodes and high quality ohmic contacts on the order of 3 ohms were obtained. Both spontaneous and lasing emission spectra of these lasers were studied at different driving currents, and transition energies of the quantum well were obtained. Obtained values were compared with the previous works and the theory. Multi-mode operation around 7972 Å wavelength was observed in lasing emission spectra. From spontaneous emission spectra second level transition was shown. I-P characterization was done for the series of samples and differential quantum efficiencies  $\eta_D$ , threshold current values  $I_{th}$  and optimal lengths for the laser diodes of stripe width 5 and 12 μm were obtained. Quantum efficiencies for one facet up to 26.7 % were obtained for cavity length of 563 μm lasers. Minimum threshold value of 18 mA was obtained for 5 μm width 295 μm long cavity laser. At 2  $I_{th}$  driving currents power output of 10 mW was easily obtained from one mirror without any reflection coating. Although uniformity inhomogenities of the laser stripes was concluded from the obtained  $J_{th}$  current densities, good far and near field characteristics show that our lasers operate in the fundamental mode of TEM<sub>00</sub> with narrow divergence of 5° in lateral and 45° in transverse directions.

Due to the limited variety of available gases suitable for dry etching, freon-12 was used for mesa formation. The low etching rate of this gas causes etching times up to an hour which is detrimental to laser structures: Indeed photoresist masks of 5 μm stripes were observed to flow during this procedure resulting in not so straight stripes. It is advisable to lower this damage by using chlorine based plasma where very high etching rates can be achievable without using high self bias voltages. In PECVD step applying low substrate temperature (100°C) depositions was found to be very useful, since it lowers the masking steps in the process and also give the ability of obtaining self aligned structures.

It is known that anti reflection coatings increase the differential quantum efficiency and the power output of the laser diodes. From the I-P characterization data, it seems that very high power lasers up to few hundred milliwatts might be achievable with anti reflection coatings after the lasers are mounted onto heat sinks. In this kind of applications using laser diode lenses on the laser mount offers much better beam characteristics. Dynamical characteristics of these lasers and tunability to single wavelength by external holographic gratings can be new research studies in the light of this thesis.

# Bibliography

- [1] N.G. Basov, O.N. Kroklin and Y.M. Popov, Production of negative temperature states in p-n junctions of degenerate semiconductors, Sov. Phys. JETP 13 (1961).
- [2] R.N. Hall, G.E. Fenner, J.D. Kingsley, T.J. Soltys and R.O. Carlson, Coherent light emission from GaAs p-n junctions, Phys. Rev. Lett. 9, Nov. (1962).
- [3] M.I. Nathan, W.P. Dumke, G. Burns, F.H. Dill and G.J. Lasher, Stimulated emission of radiation from GaAs p-n junctions, Appl. Phys. Lett. 1, Nov. (1962).
- [4] T.M. Quist, R.H. Rediker, R.J. Keyes, W.E. Krag, B. Lax, A.L. McWhorter and H.J. Zeiger, Semiconductor maser of GaAs, Appl. Phys. Lett. 1, Dec. (1962).
- [5] N. Holonyak Jr., and S.F. Bevacqua, Coherent (visible) light emission from GaAsP junctions, Appl. Phys. Lett. 1, Dec. (1962).
- [6] T.H. Maiman, Stimulated optical emission in fluorescent solids, Phys. Rev. 123 (1961).
- [7] A. Javan, W.R. Bennett Jr., and D.R. Herriot, Continuous optical maser oscillation in a gas discharge, Phys. Rev. Lett. 6 (1961).

- [8] Zh.I. Alferov, V.M. Andreev, V.I. Korolkov, E.L. Portnoi and D.N. Tretyakov, Injection properties of n-AlGaAs p-GaAs heterostructures, *Fiz. Tekh. Poluprov* 2 (1968) ; *Sov. Phys. Semicond.* 2 (1969).
- [9] H. Kroemer, *Proc IEEE* 51, 1963 1782.
- [10] Zh. I. Alferov and R.F. Kazarinov, Authors certificate 1032155/26-25 USSR (1963).
- [11] Tsang W. T., *Appl. Phys Lett.*, 39 786 (1981a), *Appl. Phys Lett.*, 39 134 (1981b).
- [12] Fusji T., Yamakoshi S., Nanbu K., Wada O., Hiyamizu S, *J. Vac. Sci. Technol.* 2,259 (1984).
- [13] Chin R., Holonyak N.Jr., Kobas R.M., Rossi J.A., Keune D.L., Groves W.O., *J.Appl. Phys.* 49,2551 (1978).
- [14] Hess K., Voyak B.A., Holonyak H.,Jr., Chin R., Dapkus P.D., *Solid State Electron* 23,582 (1980).
- [15] Arakawa Y., and Sakaki H., *Appl. Phys. Lett.* 40,939 (1982).
- [16] Arakawa Y., Vahala K., Yariv A., *Appl. Phys. Lett.* 45,950 (1984).
- [17] Arakawa Y., Yariv A., *J. Quantum Electron.*, QE-21, 1666 (1985).
- [18] Rezek E. A., Holonyak N., Jr., Vojak B. A., Stillman G.E., Rossi J.A., Keune D.L., and Fairing J.D., *Appl. Phys. Lett.* 31,288 (1977).
- [19] Dupuis R. D., and Dapkus P.D., *Appl. Phys. Lett.* 32,406 and 32,473 (1978).
- [20] Dupuis R. D., Mouldy L.A., and Dapkus P.D., *Gallium Arsenide and Related Compounds Institute of Physics, London* p.1 (1979).
- [21] Kazarinov A.K., and Tsarenkov G.V., *Sov. Phys. Semicond.* 10,178 (1976).

- [22] Hersee S.D., Baldy B., Cremoux de B., and Duchemin J.P., *Inst. Phys. Conf. Series.* 65,281 (1980).
- [23] Dutta N.K., Nelson R.J., *J. Quantum Electron QE-18*, 375 (1982).
- [24] Asada M., Kameyama A., and Suematsu Y., *J. Quantum Electronics QE-20*, 745 (1985).
- [25] Arakawa Y., Yariv A., *J. Quantum Electronics QE-22*, (1987).
- [26] Hersee S.D., Cremoux de. B., Duchemin J.P., *Appl. Phys. Lett.* 44,476 (1984).
- [27] Tsang W.T., *Appl. Phys. Lett.* 40,217 (1982).
- [28] Heinz J., Gian L.B., Peter B., Heinz P.M., William J.K., and Wilfried L., Very high power AlGaAs sqw-grinsch ridge laser with frequency-doubled output, *J. Quantum Electronics* 27,6, June (1991).
- [29] J.R. Sheally, High efficiency superlattice grinsch lasers with AlGaAs single quantum wells, *Appl. Phys. Lett.* 52,18 (1988).
- [30] Derry P.L., Yariv A., Lau k.y., Bar-Chaim N., Lee K. and Rosenberg J., *Appl. Phys. Lett.* 50,1773 (1987).
- [31] Hartman L.T., Tsang W.T., *Appl. Phys. Lett.* 42,551 (1983).
- [32] Tsang W. T., Hartman R. L., *Appl. Phys. Lett.* 42,551 (1983).
- [33] M. Jaros, *Physics and Applications of Semiconductor Microstructures*, Oxford Science Publications.
- [34] Sadao Adachi, GaAs,AlAs and  $\text{Al}_x\text{Ga}_{1-x}\text{As}$  ; Material parameters for use in research and device applications, *J. Appl.Phys.* 58,3 (1985).
- [35] M.S. Tyagi, *Introduction to Semiconductor Materials and Devices*, John Willey & Sons.

- [36] Dingle R., Wiegman W., Henry C. H., Phys. Rev. Lett. 38,827 (1987).
- [37] Dingle R., Advances in solid state physics, Pergamon Press.
- [38] E.O. Kane, J. Phys. Chem. Solids 1,249 (1957).
- [39] R.K. Willardson and A.C. Beer, Semiconductors and semimetals, Academic press.
- [40] G. Duggan, A critical review of heterojunction band offsets, J. Vac. Sci. Technol., B,3 (1985)
- [41] Ralph E. Williams, Modern GaAs processing methods, Artech House.
- [42] R. Henderson, Electron beam technology in micro electronic fabrication, Academic Press.
- [43] K. Levy and P. Sadland, Solid State Technology, May (1978).
- [44] Wayne M. Moreau, Semiconductor lithography principles, practices and materials, Plenum Press.
- [45] M. Bolsen, G. Buhr, H. Merrem and K. Van Werden, Solid State Technology, February (1986).
- [46] Bob Mohondro, Resist adhesion promoter application, European Semiconductor, November (1991).
- [47] C.M. Melliar-Smith and C.J. Mogab, Thin film processes, Academic Press.
- [48] F.N. Timofeev, Reactive ion etching for fabrication of integrated optic and optoelectronic elements, A.I.P. Conference Proceedings 240.
- [49] S.J. Moss and A. Ledwith, The chemistry of the semiconductor industry, Blackie.
- [50] A. Kiermasz, Andrew Chambers and Andrew McQuarrie, Research & Development December (1987).



- [51] P.A. Longeway, R.D. Estes and H.A. Weakliem, *J.Phys. Chem.* 88,73 (1984).
- [52] P.D. Richard, R.J. Markunas, G. Lucovsky, G.G. Fountain, A.N. Mansous and D.V. Tsu, *J.Vac.Sci.Tech. A* 3,867 (1985).
- [53] G. Lucovsky, P.D. Richard, D.V. Tsu, S.Y. Lin and R.J. Markunas, *J.Vac.Sci.Tech. A* (proceedings).
- [54] G. Smolinsky and T.P.H.F. Wendling, *J.Electrochem.Soc. , Solid State Science and Tech.* April (1985).
- [55] J. Bell and P. Dean, *Discuss. Faraday Soc.* 50,55 (1970).
- [56] C.K. Wong, G. Lucovsky and W.B. Pollard, *J.Non-Cryst. Solids* 59,60,869 (1983).
- [57] G. Lucovsky, M.J. Mantini, J.K. Srivastava and E.A. Irene, Low temperature of silicon dioxide films: A study of chemical bonding by ellipsometry and infrared spectroscopy, *J.Vac.Sci.Technol. B* 5,2 Mar/Apr (1987).
- [58] D.V. Tsu, G. Lucovsky, M.J. Mantini and S.S. Chao, *J.Vac.Sci.Technol. A* 5,1988 (1987).
- [59] P.G. Pai, S.S. Chao, Y. Takagi and G. Lucovsky, *J.Vac.Sci.Techol. A* 4,689 (1986).
- [60] R.A.B. Devine, On structure of low temperature PECVD SiO<sub>2</sub>-films, *Journal of Electronic Materials* 19,11 (1990).
- [61] Feodor N. Timofeev, (unpublished), Private Communications December (1994).
- [62] *European Semiconductor*, October (1992).

- [63] Jacques I. Pankove, Optical processes in semiconductors, Dover Publications.
- [64] Mitsuhiro Yano, Hiroshi Nishi and Masahito Takusagawa, J. Quantum Electronics QE-15,7 (1979).
- [65] E. Zielinski, H. Schweizer, S. Hausser, R. Stuber, M.H. Pilkuhn and G. Weimann, Systematics of laser operation in GaAs/AlGaAs multiquantum well heterostructures, IEEE J. Quantum Electron QE-23,pp 969-976 (1987).
- [66] P. Blood, E.D. Fletcher, P.J. Hulyer and P.M. Smowton, Emission wavelength of AlGaAs/GaAs multiple quantum well lasers, Appl. Phys. Lett. 48, pp 1111-1113 (1986).
- [67] Stephen R. Chinn, Peter S. Zory and Axel R. Reisinger, A model for GRIN-SCH-SQW diode lasers, J.Quantum Electronics 24,11, Nov (1988).
- [68] Basil W. Hakki and Thomas L. Paoli, Gain spectra in GaAs double-heterostructure injection lasers, J. Appl. Phys. 46,3, March (1975).
- [69] Morris P. Kesler and Christoph Harder, Spontaneous emission and gain in GaAlAs quantum well lasers, J. Quantum Electronics 27,6 June (1991)
- [70] W.T. Tsang, A graded index waveguide separate-confinement laser with very low threshold and a narrow Gaussian beam, Appl. Phys. Lett. 39,2, July (1981)
- [71] A. Kurobe, H. Furuyama, S. Naritsuka, N. Sugiyama, Y. Kokubun, and M. Nakamura, Effect of quantum well number, cavity length, and facet reflectivity on the reduction of threshold current of GaAs/AlGaAs multiquantum well lasers, J. Quantum Electronics 24,4, April (1988).
- [72] M. Mittelstein, Y. Arakawa, A. Larsson and A. Yariv, Second state lasing of a current pumped single quantum well laser, Appl. Phys. Lett. 49,25, Dec. (1986).

- [73] Stephen R. Chinn, Modal Analysis of GRINSCH and triangular-well waveguides, *Applied Optics* 23,20 Oct. (1984).